RRB-87-10

REMOTE AND IN SITU OPTICAL STUDIES OF SESTON AND SUSPENDED SEDIMENT CONCENTRATIONS IN LAKE ST. CLAIR

by
R.P. Bukata, J.H. Jerome and J.E. Bruton

Rivers Research Branch
National Water Research Institute
Canada Centre for Inland Waters
Burlington, Ontario, Canada

February 1987
NWRI Contribution #87-42

MANAGEMENT PERSPECTIVE

The use of ship surveys defined by a pre-determined optimal set of discrete sampling stations has long been recognized as being an indisputably essential component of programs seriously dedicated to the monitoring and assessment of the bio-chemical/physical properties of large lake and river systems. While the contributions of discrete point sampling programs are of inarguable value, such point sampling activities are forced to contend with at least one severe limitation, namely the loss of comparable information for aquatic regimes between the discrete sample stations. These discontinuities in the time-space continuum could result in serious uncertainties being reflected within the deductions based on discrete sampling information, particularly when such discrete sampling activities are performed on aquatic resources subjected to short-term fluctuations and/or large scale variations in any or all of the physical, chemical, and biological parameters comprising their makeup.

This communication describes a ship-mounted optical device which is intended to supplement, in certain situations, the discrete sampling ship surveys, by providing the capability to continuously monitor, in a remote manner, the aquatic resource while the research vessel is in transit between the fixed monitoring stations. The ship-mounted remote sensing device is a Multispectral Optical Monitoring System (MOMS) comprised of an upward-viewing four-channel radiometer subsystem with rotating solar occluder (which continually monitors the downwelling solar and sky irradiance) and a downward-viewing four-channel radiometer subsystem (which continually monitors

the upwelling radiance from the water). An optical model is developed which allows the conversion of the downwelling irradiances and upwelling radiances into spectral values of the subsurface irradiance reflectance (volume reflectance) normalized to a standard solar zenith angle and a standard downwelling light field. This normalized multispectral subsurface volume reflectance is then utilized to evaluate the capability of effectively conducting, from a moving research vessel, a continuous monitor of the total seston and suspended sediment concentrations in the generally turbid, shallow waters of Lake St. Clair. Examples of ship/MOMS transects of Lake St. Clair are presented which display very good agreement between the laboratory-analyzed concentrations of seston and suspended sediments from collected samples, and between-station concentrations remotely estimated by the continuous optical data collected and interpreted by MOMS.

In addition to remote optical monitoring being of value in assessing the water quality indicators of inland lakes, in situ optical techniques also possess certain capabilities which enable estimates to be made of the nature and density of aquatic scattering and absorption centres. This communiciation deals with the use of optical transmission profiles (which yield measures of the total attenuation coefficients) to estimate seston and suspended sediment concentrations in Lake St. Clair.

Both the in situ transmission and remote upwelling radiance measurements of Lake St. Clair display a high degree of mutual interconsistency.

PERSPECTIVE - GÉSTION

Il est reconnu depuis longtemps que les relevés en navire d'un ensemble optimal de points d'échantillonnage discontinu et prédéterminé sont essentiels dans la surveillance et l'évaluation des propriétés biochimiques et physiques des eaux des grands lacs et des grands cours d'eau lorsqu'on veut faire un travail sérieux. L'utilité de ces relevés est incontestable, mais l'échantillonnage discontinu présente au moins un grand inconvénient : on n'obtient aucune donnée comparable sur les régimes aquatiques entre chaque point de relevé. Ces intervalles dans l'espace et le temps peuvent être à l'origine d'incertitudes importantes, incertitudes qui influeront sur les déductions qu'on pourra faire à l'analyse des renseignements recueillis, surtout si l'on étudie un milieu aquatique dont certaines des caractéristiques physiques, chimiques et biologiques, sinon toutes, fluctuent rapidement ou varient beaucoup.

On décrit ici un appareil optique qui se monte sur le navire de recherche et qui devrait permettre de compléter, dans certaines conditions, les résultats des relevés ponctuels en donnant la possibilité de surveiller continuellement le milieu aquatique par télédétection, alors que le navire de recherche se déplace entre deux points de contrôle. Il s'agit de l'appareil de surveillance optique multispectral (ASOM) : il se compose d'un radiomètre à quatre canaux avec obturateur solaire, orienté vers le haut (qui permet de contrôler le rayonnement solaire et la lumière du ciel) et d'un radiomètre à quatre canaux, orienté vers le bas (qui permet de contrôler les rayonnements ascendants dans l'eau). On est à mettre au point un modèle optique pour convertir l'énergie des rayonnements descendants et ascendants en valeurs de luminance spectrale dans la couche sous-jacente (luminance de volume) normalisées en fonction d'un angle de zénith et d'un champ lumineux standard. La luminance de volume sous-jacente multispectrale normalisée sert à déterminer avec quelle efficacité on peut contrôler en continu, depuis le navire de recherche en mouvement, les concentrations totales de seston et de matières solides en suspension dans les eaux peu profondes, généralement troubles, du lac Sainte-Claire. On donne des exemples de transects contrôlés au moyen de l'ASOM dans le lac Sainte-Claire pour montrer que les concentrations de seston et de matières solides en

suspension mesurées en laboratoire dans les échantillons recueillis concordent très bien avec les valeurs déterminées par contrôle optique continu en télédétection au moyen de l'ASOM.

Outre le fait que surveillance optique par télédétection est utile pour évaluer les indicateurs de la qualité de l'eau des lacs, les techniques d'observation optique in situ permettent de faire des estimations au sujet de la nature et de la densité des points de diffusion et d'absorption en milieu aquatique. On explique comment on s'est servi de profils de transmission optique (qui permettent de mesurer les coefficients d'atténuation totale) pour estimer les concentrations de seston et de matières solides en suspension dans les eaux du lac Sainte-Claire.

On a noté une grande concordance entre la transmission mesurée in situ et les rayonnements ascendants mesurés par télédétection dans le lac Sainte-Claire.

ABSTRACT

Initial results of an optical study of the relatively turbid waters of Lake St. Clair performed in 1985 are presented and discussed. The optical study included both *in situ* transmission profiling, and remote measurements of upwelling spectral radiance.

Methodology is developed to convert the upwelling multispectral radiance observed by a ship-mounted dual radiometer reflectance system into the subsurface volume reflectance normalized to a standard solar zenith angle and a standard downwelling light field. This normalized multispectral subsurface volume reflectance is then utilized to evaluate the capacity of effectively conducting, from a moving research vessel, a continuous monitor of the total seston and suspended sediment concentrations in the generally turbid, shallow waters of Lake St. Clair. Good agreement is obtained between remotely predicted and directly sampled concentrations of both seston and suspended sediments.

Regressions between the total attenuation coefficient and both the seston and suspended sediment concentrations are also presented and discussed, as are the consistencies observed between the direct and remote optical monitoring and modelling activities conducted on Lake St. Clair.

RÉSUMÉ

On présente les premiers résultats d'une étude optique portant sur les eaux relativement troubles du lac Sainte-Claire. Les travaux, réalisés en 1985, consistaient à dresser des profils de transmission au moyen de mesures faites *in situ* et à mesurer les rayonnements spectraux ascendants par télédétection.

On est à mettre au point la méthodologie de la conversion de l'énergie des rayonnements ascendants observés au moyen d'un appareil de radiométrie double monté sur un navire en valeurs de luminance de volume sous-jacente normalisées en fonction d'un angle de zénith et d'un champ lumineux descendant standard. Ces valeurs servent à déterminer avec quelle efficacité on peut contrôler en continu, depuis un navire de recherche en mouvement, les concentrations totales de seston et de matières solides en suspension dans les eaux peu profondes et généralement troubles du lac Sainte-Claire. Les concentrations de seston et de matières solides en suspension mesurées en laboratoire concordent bien avec les valeurs déterminées par télédétection.

On présente aussi les résultats des analyses de régression qu'on a réalisées pour évaluer la concordance entre le coefficient d'atténuation totale et les concentrations de seston et de sédiments en suspension et entre les mesures et les modèles optiques obtenus par observation directe et par télédétection dans le lac Sainte-Claire.

INTRODUCTION

The importance of Lake St. Clair (located in the middle of the aquatic transport avenue between Lake Huron and Lake Erie), both as a sediment trap and an aquatic flow-through between the Upper and Lower Great Lakes, has prompted extensive Canadian and American studies in recent years. This report presents some initial results of an optical study of the shallow waters of Lake St. Clair performed during the May to November 1985 field season. The optical study included direct subsurface measurements of optical transmission, as well as remote upwelling radiance measurements obtained from a shipborne Multispectral Optical Monitoring System (MOMS).

MOMS is comprised of dual radiometer reflectance assemblies. One radiometer views the upper hemisphere while the other has a viewing direction vertically downwards. Analysis and interpretation methodologies are derived and discussed. These methodologies attempt to relate the solar and sky irradiance data collected continually by the upward-viewing radiometer, along with the upwelling radiance collected continuously by the downward-viewing radiometer into subsurface volume reflectance values which can be used to remotely estimate the seston and suspended sediment concentrations present in the lake.

Being a ship-mounted spectral radiometer system, MOMS, in essence, represents an extremely slow moving, low-altitude, orbiting environmental satellite that affords the opportunity for a quasi-continuous water quality monitoring activity.

IN-SITU TRANSMISSION MEASUREMENTS IN LAKE ST. CLAIR

Figure 1 illustrates a schematic map of Lake St. Clair upon which is superimposed a set of fixed surveillance stations at which water samples were collected and laboratory analyzed for total seston and suspended sediment concentrations. In situ optical transmission measurements were also performed at these stations utilizing a 0.25 m path length Martek XMS transmissometer equipped with a Wratten 45 filter (0.485 μ). The research vessel CSS LIMNOS made nine separate visitations (at approximately three week intervals) to these stations between June 5 and November 17, 1985. At each station visitation, transmission and temperature profiles were obtained within the water column. Seston and suspended sediment concentrations were determined at depths of 1 metre below the surface and 1 metre above the bottom with intermediate samples collected if vertical structuring was indicated from the thermal profile at the station.

From the transmission profiles, the total attenuation coefficient c (in units of m^{-1}) at the water sampling depth was determined from the equation

$$c(z) = \ln [100/T(z)]^4 \qquad (1)$$

where T(z) is the percent transmission over 0.25 m path length recorded at sampling depth z.

In an attempt to separate the optical effects of the organic and inorganic components of the suspended materials, a multiple regression was performed among the attenuation coefficient, the organic component of the suspended load (estimated as being the difference between seston concentration and suspended sediment concentration), and the inorganic component of the suspended load (estimated as being appropriately represented by the suspended sediment concentration). From such a regression, the total attenuation coefficient c(z) was related to the organic and inorganic components in the following manner:

$$c(z) = 0.30 + 0.71\ SS(z) + 0.46\ SO(z) \qquad (2)$$

where SS(z) and SO(z) are the concentrations in g m^{-3} at depth z of the suspended sediment and suspended organic components, respectively.

From equation (2) it is seen that a fixed concentration of suspended sediment (i.e. inorganic material) will produce a comparable attenuation to a suspended organic material concentration 1.5 times as large. This is probably a direct consequence of the inorganic suspended sediments being characterized by a smaller average particle size than the organic suspended load.

In order to utilize measurements of total attenuation coefficient c(z) as a means of predicting seston and suspended sediment concentrations in the absence of direct water sample collection,

correlations between c(z) and seston and between c(z) and suspended sediments were performed. These correlations are illustrated in Figures 2 and 3, respectively. The correlation between c(z) and seston concentration S(z) may be mathematically expressed as

$$S(z) = 0.08 + 1.35\ c(z) \tag{3}$$

with correlation coefficient r=0.96 and standard deviation of the errors $\sigma=\pm 15\%$.

The correlation between c(z) and suspended sediment concentration SS(z) may be mathematically expressed as

$$SS(z) = -0.52 + 1.21\ c(z) \tag{4}$$

with r=0.96 and $\sigma=\pm 16\%$.

Equations (3) and (4) may be considered to represent partial correlations of the independent variables S(z) and SS(z) with the dependent variable c(z) assuming that for each value of the independent variable considered, the ratio of the two independent variables remains a constant, i.e. that homogeneity with respect to the relative concentrations of seston and suspended sediments is preserved throughout the aquatic region under study.

It may further be reasoned that the intercept term in equations (3) and (4) should be zero or negative. This is due to the fact that

even for situations in which the water mass contains no particulate loading (i.e $S(z) = SS(z) = 0$), the value of $c(z)$ must still remain positive to allow for the attenuation of the pure water plus dissolved load remaining within the water mass. Equation (4) satisfies this condition, while equation (3) mildly violates this condition. However, the intercept term in equation (3) is close to zero, and the intercept value 0.08 g m^{-3} is of the order of the uncertainties encountered in the laboratory determinations of the concentrations measured in the current study of Lake St. Clair.

It must be noted that equations (2), (3) and (4) are appropriate to the conditions existing in Lake St. Clair at the time of experiment execution (summer/autumn field season, 1985). Consequently, caution must be exercised in attempting to apply such results to other sites and/or other environmental conditions. However, Bukata et al (1985a) illustrate the relationship of $c(z)$ and $SS(z)$ obtained for Lake Erie in 1975. The correlations independently obtained in Lake Erie and Lake St. Clair a decade apart, are remarkably similar. The equation describing the 1975 Lake Erie correlation between $c(z)$ and $SS(z)$ may be written

$$SS(z) = -0.22 + 1.10\ c(z) \qquad (5)$$

The differences between $SS(z)$ predicted from equation (5) for Lake Erie and equation (4) for Lake St. Clair over the range $2\ m^{-1} \leq c(z) \leq 12\ m^{-1}$ are <7%.

MULTISPECTRAL OPTICAL MONITORING SYSTEM (MOMS)

MOMS is a duo-directional radiometer reflectance system, continuously operable and ship-mounted so that one radiometer views the upper hemisphere, while the other radiometer has a viewing direction vertically downwards. In essence, therefore, MOMS represents an extremely slow moving, low-altitude orbiting environmental satellite which affords the opportunity for a quasi-continuous water quality monitoring activity.

Figure 4 illustrates a schematic representation of this ship-mounted remote sensing device. Each of the radiometer subsystems consists of a commercial Exotech radiometer with a four-channel spectral capability. The spectral bands correspond to those of the LANDSAT/THEMATIC MAPPER blue, green and red bands and the LANDSAT/MULTISPECTRAL SCANNER infra red band in the wavelength intervals (0.45 μ - 0.52 μ), (0.52 μ - 0.60 μ), (0.63 μ - 0.69 μ), and (0.8 μ - 1.1 μ), respectively. The upward-viewing subsystem, designed to obtain data on the variability of incident radiation conditions, is equipped with an enclosing hemispherical plexiglass window and a rotating solar occluder assembly. The field of view of the upward-viewing radiometer assembly is 2π sterads, cosinusoidal, and the solar occluder rotation period of 45 seconds allows for the continual monitoring of total (direct and diffuse) and diffuse incident spectral irradiance. The field of view of the downward-viewing radiometer assembly is 15° corrected for ship's roll

and pitch, and thus allows for continuous monitoring of the near surface upwelling spectral radiance from the lake water.

Detailed descriptions of the electro-optical, mechanical, and physical characteristics of MOMS, along with installation and mounting details, operating procedures and performance specifications and indicators, functional block and wiring diagrams, and data acquisition and storage techniques may be found in the report by Watson et al. (1982).

If H_{sun} and H_{sky} represent the spectrally-dependent downwelling irradiances from the sun and sky, respectively, and H_{LOW} and H_{HIGH} represent the spectrally-dependent downwelling irradiances recorded by the upward-viewing radiometer assembly with the solar occluder blocking and not blocking the solar disk from the sensor's field of view, respectively, then it is evident that

$$H_{sun} = (H_{HIGH} - H_{LOW})/T_{COVER} \quad (6)$$

and

$$H_{sky} = H_{LOW} /mT_{COVER} \quad (7)$$

where

T_{COVER} = transmission of the hemispherical plexiglass cover plate

m = fraction of sky not occluded

The upwelling radiance L_{Up} from the surface is given by

$$L_{Up} = H_{UpW}\, T_{SURF}/Q + f_1\, H_{sky}\, f_2\, H_{sun} \qquad (8)$$

where H_{UpW} = upwelling irradiance below the water surface

Q = ratio of upwelling irradiance below the water surface to the upwelling nadir radiance below the water surface

T_{SURF} = transmission of nadir radiance through the air-water interface including correction for the n^2 radiance law (n being the relative refractive index of the water)

f_1 = ratio of the upwelling radiance entering the FOV of the sensor (originating from surface-reflected diffuse skylight) to the downwelling sky irradiance

f_2 = ratio of the upwelling radiance entering the FOV of the sensor (originating from surface-reflected direct sunlight) to the downwelling solar irradiance.

From equation (8), the upwelling irradiance below the water surface is given by

$$H_{UpW} = Q\,[L_{Up} - f_1\, H_{sky} - f_2\, H_{sun}] \,/\, T_{SURF} \qquad (9)$$

The downwelling irradiance H_{DnW}, below the water surface is given by

$$H_{DnW} = f_3 H_{sky} + f_4 H_{sun} \qquad (10)$$

where f_3 = fraction of downwelling sky irradiance transmitted into the water

f_4 = fraction of downwelling solar irradiance transmitted into the water

The spectrally-dependent diffuse irradiance reflectance or volume reflectance R_V, just beneath the surface of the water, is then obtained as the ratio of equation (4) to equation (5), i.e.

$$R_V = \frac{H_{UpW}}{H_{DnW}}$$

$$= \frac{Q[L_{Up} - f_1 H_{sky} - f_2 H_{sun}]}{T_{SURF}[f_3 H_{sky} + f_4 H_{sun}]} \qquad (11)$$

In order to facilitate the conversion of the above surface optical parameters L_{Up} (upwelling spectral radiance), H_{sky} (downwelling sky irradiance), and H_{sun} (downwelling solar irradiance) directly measured by MOMS, into the subsurface optical parameter R_V (volume reflectance), not directly measured but required to infer the scattering and absorption processes occurring within the water column, it is convenient to express the fractions f_1, f_2 f_3, and f_4 in the following terms:

$$f_1 = \alpha \rho_o + \beta_1 \qquad (12)$$

where α = the spectrally-dependent ratio of downwelling zenith sky radiance to downwelling sky irradiance

ρ_0 = Fresnel reflectivity for vertical incidence (i.e. zenith angle of 0°)

β_1 = ratio of the upwelling radiance entering the FOV of the sensor (a consequence of sky irradiance being reflected by surficial waves) to the downwelling sky irradiance.

From Gordon (1969), the value of β_1 for wind speeds of 0-10 m sec^{-1} is taken to be zero. Since this condition is satisfied throughout this investigation, equation (12) may be simplified to

$$f_1 = \alpha \rho_0 \qquad (13)$$

The Fresnel reflectivity ρ_0 at $\theta = 0°$ is 0.0212 for a relative index of refraction n=1.341. Equation (13) then becomes

$$f_1 = 0.0212 \alpha \qquad (14)$$

An expression for f_2 (reflection of solar irradiance due to surficial waves) may be obtained for waters displaying small to moderate suspended sediment concentrations by assuming that the volume reflectance response in the near infra-red wavelengths may be confidently taken to be zero. For this condition, the infra-red radiance response L_{Up} may be written

$$L_{Up} = f_1 H_{sky} + f_2 H_{sun}$$

from which

$$f_2 = \frac{L_{Up} - H_{sky} \rho_o \alpha}{H_{sun}} \qquad (15)$$

where L_{Up}, H_{sky}, H_{sun}, and α are the appropriate values of these parameters for the infra-red channel.

For the case of highly sediment-laden waters such as typically comprise Lake St. Clair, however, the assumption of zero volume reflectance observable just above the air-water interface for near-infra-red wavelengths is not valid. Consequently, equation (15) is not applicable to Lake St. Clair.

As described in Maul (1985), the radiance reflected from the water surface due to wave action ($f_2 H_{sun}$) may be expressed as

$$f_2 H_{sun} = \frac{\rho(\omega) H_{sun} \exp[-\frac{\tan^2\delta}{S^2}]}{4\pi S^2 \cos\psi \cos^4\delta}$$

from which

$$f_2 = \frac{\rho(\omega) \exp[-\frac{\tan^2\delta}{S^2}]}{4\pi S^2 \cos\psi \cos^4\delta} \qquad (16)$$

where ω = solar angle of incidence causing reflection into the FOV of the sensor

$\rho(\omega)$ = Fresnel reflectivity for incident angle ω

ψ = zenith angle of the sensor (0° for the configuration considered herein)

δ = wave slope required to produce observable solar glitter at the sensor

S^2 = mean square wave slope

Ambient conditions under which MOMS was utilized in Lake St. Clair included a) a range of solar zenith angles 40° to 65° (resulting in ω values ranging from 20° to 32.5°) and b) maximum wind speeds of 5 m sec^{-1}. These conditions resulted in negligible values of f_2 ranging from 8.3×10^{-8} to 7.1×10^{-4}. Therefore, for this study f_2 was confidently taken to be zero, suggesting that surface glitter from the sun was not even a minor contributor to the measured above water radiance.

$$f_3 = 1 - (\rho_{sky} + \beta_3) \qquad (17)$$

where ρ_{sky} = Fresnel reflectivity of the sky irradiance

β_3 = fraction of sky irradiance which is reflected due to surficial waves (β_3 is a negative fraction in this instance since the wave action serves to inhibit reflection from its surface)

From Jerlov (1984), ρ_{sky} may be considered to have the value 0.066. Values of β_3 are related to wind speed and possess values of -0.010 for a wind speed of 4 m sec^{-1} (Payne, 1972) and -0.014 for a wind speed of 7 m sec^{-1} (Cox and Munk, 1955). For the current work a value of $\beta_3 = -0.010$ was used. From equation (17), this yields a value of $f_3 = 0.944$.

$$f_4 = 1 - (\rho(\theta) + \beta_4) \tag{18}$$

where $\rho(\theta)$ = Fresnel reflectivity of solar irradiance for solar zenith angle θ

β_4 = fraction of solar irradiance which is reflected due to surficial waves

From Cox and Munk (1955), the term $(\rho(\theta) + \beta_4)$ may be mathematically expressed as the series

$$\rho_w(\theta) = \rho(\theta) + \beta_4 = \rho(\theta) \left\{\frac{1}{2}\left[1 + I(k)\right] + \frac{1}{2}\pi^{-\frac{1}{2}} aSe^{-k^2} + \frac{1}{4} bS^2 \left[1 + I(k) - 2\pi^{-\frac{1}{2}} ke^{-k^2}\right] + \frac{1}{4} cS^2 \left[1 + I(k) + \ldots\ldots\ldots\right]\right\} \tag{19}$$

where S^2 = mean square wave slope

= 0.003 + (0.512 x 10^{-2} x wind speed)

k = $(2S)^{-1}$ cot θ

$$I(k) = 2\pi^{-\frac{1}{2}} \int_0^k e^{-t^2}\, dt$$

$$F = \rho(\theta) \cos \theta$$

$$a = \frac{1}{F} \frac{dF}{d\theta}$$

$$b = \frac{1}{2} + \frac{1}{2F} \frac{d^2F}{d\theta^2}$$

$$c = \frac{1}{2} + \frac{\cot\theta}{2F} \frac{dF}{d\theta}$$

Therefore, $f_4 = 1 - \rho_w(\theta)$ (20)

Collecting equations (12), (16), (17), and (20) and substituting into equation (11) yields the general expression for the spectrally-dependent volume reflectance R_v observable just below the water surface

$$R_V = \frac{Q\{L_{Up} - (\alpha\rho_0 + \beta_1) H_{sky} - \frac{\rho(\omega)\exp[-\frac{\tan^2\delta}{S^2}] H_{sun}}{4\pi S^2 \cos\psi \cos^4\delta}\}}{T_{SURF}\{[1 - (\rho_{sky} + \beta_3)] H_{sky} + [1 - \rho_w(\theta)] H_{sun}\}} \quad (21)$$

Simplifying the general equation (21) into a particular equation applicable to the b_1, f_2, β_3 and β_4 values pertinent to the current investigation yields

$$R_V = \frac{Q\{L_{Up} - 0.0212\,\alpha\, H_{sky}\}}{T_{SURF}\{0.944\, H_{sky} + [1 - \rho_w(\theta)] H_{sun}\}} \quad (22)$$

From the MOMS sensor configurations and physical properties, the transmission of the hemispherical plexiglass cover, T_{COVER} was

measured to be 0.923 and the fraction of the sky m not occluded by the rotating occluder was 0.9497. A value of T_{SURF} = 0.544 for a relative index of refraction of 1.341 was chosen (Duntley et al. 1974). The governing equation for the data collected remotely by MOMS over Lake St. Clair thus becomes:

$$R_V = \frac{Q\,(L_{Up} - 0.0242\,\alpha\,H_{LOW})}{0.5859\,H_{LOW} + 0.5894\,[1 - \rho_w(\theta)]\,(H_{HIGH} - H_{LOW})} \qquad (23)$$

where L_{Up} is the spectrally-dependent values of upwelling radiance recorded continuously by the downward-viewing four-channel radiometer assembly, H_{HIGH} and H_{LOW} are the spectrally-dependent values of downwelling irradiance recorded continuously by the periodically solar-occluded upward-viewing four-channel radiometer assembly, Q is the ratio of upwelling irradiance below the water surface to the upwelling nadir radiance below the water surface, α is the spectrally-dependent ratio of downwelling zenith sky radiance to downwelling sky irradiance, and $\rho_w(\theta)$ is the solar irradiance reflectance term given by equation (19). Each of Q, α, and $\rho_w(\theta)$ must be calculated for each of the R_V values to be determined.

Values of α were obtained through empirical relationships between sky irradiance and zenith sky radiance obtained prior to the on-board use of MOMS. Both of the four-channel radiometer assemblies were positioned in an upward-viewing configuration. In such a configuration the normally upward-viewing irradiance system continued to monitor the downwelling irradiances, while the normally downward-

viewing radiance system enabled a simultaneous monitoring of the zenith sky radiance.

Monte Carlo simulations of radiative transfer processes were used to estimate appropriate values of Q. Absorption and scattering coefficients and backscattering probabilities were varied over ranges considered to be typically representative of Great Lakes water masses (Bukata et al., 1979) and the salient results of this Monte Carlo simulation are depicted in Figure 5. Herein are plotted the estimated values of Q (upwelling irradiance below the water surface divided by that upwelling radiance just below the water surface that would refract into a 15° sensor FOV just above the water surface assuming 100% transmission through the air-water interface) against solar zenith angle θ. Curve A represents a relatively large backscattering probability (0.044) while Curve B represents a relatively low backscattering probability (0.013). The ratio of scattering to absorption was observed to possess a minimal impact on the curves of Figure 5. For the purpose of this work, Curve C which represents the arithmetic means of Curves A and B was used in the determination of Q. For the range of solar zenith angles appropriate to the Lake St. Clair measurements (40° to 65°), values of Q varied from 3.92 to 4.66 (these may be compared to the fixed value of 5.08 reported by Duntley et al. (1974), although conceivably for a detector of FOV other than 15°).

One further mathematical correction must be made to the determined value of R_y. Since the continuous MOMS data stream is collected under temporally-varying conditions of solar zenith angle θ

and relative fractions of diffuse and direct downwelling radiation, it is necessry to normalize the subsurface volume reflectance R_V to a standard solar zenith angle and a standard downwelling radiation. If the fraction of total radiation which is diffuse is denoted by F, and the fraction of total radiation which is direct is denoted by (1-F), then

$$R_V(\theta,F) = (1 - F)\, R_{VS}(\theta) + FR_{VD} \qquad (24)$$

where $R_{VS}(\theta)$ = the volume reflectance for direct downwelling radiation (R_{VS} is dependent on θ)

R_{VD} = the volume reflectance for diffuse downwelling radiation (R_{VD} is independent of θ)

Another Monte Carlo simulation was established to determine the impact on $R_{VS}(\theta)$ of varying θ. Results from the Monte Carlo simulation are illustrated in Figure 6 wherein is plotted the ratio $R_{VS}(\theta)/R_{VS}(0)$ (i.e. the ratio of the subsurface volume reflectance for a solar zenith angle θ to the subsurface volume reflectance for a solar zenith angle of 0°) as a function of the inverse of the cosine of the refracted angle θ_r. The straight line relationship is defined by

$$R_{VS}(\theta) = \frac{R_{VS}(0)}{\text{Cos } \theta_r} \qquad (25)$$

where $\theta_r = \sin^{-1}\left(\frac{\sin\theta}{n}\right)$

The value of R_{VD} from the Monte Carlo simulation was determined to be

$$R_{VD} = 1.165\, R_{VS}(0) \qquad (26)$$

Substituting equations (25) and (26) into equation (24) and rearranging terms yields

$$R_{VS}(0) = \frac{R_V(\theta,F)}{(1.165F + \frac{(1-F)}{\cos \theta_r})} \qquad (27)$$

It is this normalized value $R_{VS}(0)$ of the subsurface volume reflectance which is utilized in the current above surface investigation of the water masses comprising Lake St. Clair.

DATA SAMPLING LOGISTICS

Figure 7 illustrates a schematic map of Lake St. Clair upon which is superimposed a set of fixed water sampling stations at which water was collected and laboratory analyzed for total seston and suspended sediment concentrations. Transmission measurements were also performed at these stations utilizing a 0.25 m path length Martek XMS transmissometer equipped with a Wratten 45 filter (0.485 μ). MOMS, mounted on a 4.5 m articulated boom, was extended from the bow of the research vessel CSS ADVENT in a manner such as to maintain a 4.5 m height above the water surface for the downward-viewing radiometer assembly. Four visitations to Lake St. Clair were made during September 1985.

The 15° FOV of the radiance radiometer allows a monitoring of optical return from a circular surficial area of diameter 1.2 m. Extending MOMS a distance of 4.5 m in advance of the ship effectively

eliminates the influence of bow waves and ship shadow contamination of the sensor FOV (with the exception of solar zenith angles > 45° for the sun located directly aft).

In order to allow on-board adjustment to changing conditions of encountered water masses, MOMS is equipped with automatic gain selectors which provide each sensor with the capacity to maintain signal outputs in the mid-range of each gain setting. The voltage outputs from the assembly of eight sensors (four upward-viewing and four downward-viewing) are recorded by a Sea Data logger at a rate of 2 hertz. This recording rate enabled a measurement of L_{Up} and H_{HIGH} every 0.5 seconds and a measurement of H_{LOW} every 45 seconds.

Such continual monitoring performed from a moving vehicle results in a greatly increased volume of data sets on which analysis may be performed. This, in turn, provides the capability of obtaining considerably more spatial information than can be obtained from surveillance techniques restricted to point sampling. For an average ship speed of 10 knots, the 2 Hz sampling rate provides a data set every 2.6 metres along the ship track. A 135 m cassette data tape will record L_{Up}, H_{HIGH} and H_{LOW} for about 11 hours or 200 km of ship track.

RELATIONSHIPS AMONG SPECTRAL VOLUME REFLECTANCE, ATTENUATION COEFFICIENT, AND SESTON AND SUSPENDED SEDIMENT CONCENTRATIONS

The collection of *in situ* transmissometer profiles at the stations sampled during the MOMS surveys enabled another independent

data set to be utilized to estimate the relationship between c(z) and each of S(z) and SS(z). The transmissometer data collected during the five MOMS surveys yielded the relationships

$$S(z) = 0.32 + 1.29\ c(z) \qquad (28)$$

with $r = 0.96$ and $\sigma = \pm 15\%$

$$SS(z) = 0.29 + 1.02\ c(z) \qquad (29)$$

with $r = 0.93$ and $\sigma = \pm 19\%$

Equations (28) and (29) were determined with the exclusion of the data set obtained at Station 61 on September 14, 1985. This data set contained optical data (MOMS and transmissometer) which were internally consistent, but dramatically inconsistent with the sampled results. While equations (28) and (29) are in reasonable agreement with their counterpart equations (3) and (4) obtained during the <u>in situ</u> optical surveillance surveys, the intercepts (which should be negative values) are both significantly positive. This could be a consequence of difficulties encountered in the sampling procedures (the optical measurements being applicable to water masses distinct from the water masses being directly sampled, as will be discussed in a later section of this report. The internal consistencies of the optical measurements add further credence to this possibility.).

Further, equations (28) and (29) arose from a consideration of 42 data points while equations (3) and (4) arose from a consideration of 178 data points. More reliability is therefore ascribed to the use of equations (3) and (4) than to the use of equations (28) and (29) for relating c(z) to S(z) and SS(z).

Elsewhere (Bukata et al. 1985b) are presented detailed discussions on the complexities encountered when attempting to utilize monochromatic subsurface irradiance reflectance (volume reflectance) measurements to infer water quality parameters from natural waters displaying a wide range of concentration values for a variety of distinct scattering and absorption centres. In particular, the oftentimes total inability to extract the optical impact of chlorophyll a concentrations from the overwhelming optical influences generated by variations in the concurrent presences of suspended solids and dissolved organic substances is well illustrated. However, for water masses such as found in the shallow waters of Lake St. Clair in which the normally encountered suspended sediment concentrations are the predominant source of subsurface optical interactions, single band monochromatic volume reflectance measurements may be of considerable significance. This is particularly true, as seen from Figures 30, 31 and 32 of Bukata et al. (1985b), for the subsurface irradiance reflectance in the red wavelength region of the visible spectrum. Since the red reflectance versus suspended sediment concentration curves tend to asymptotically approach a constant reflectance for large concentrations of suspended sediments, the

maximum sensitivity of this optical parameter occurs for small to relatively moderate concentrations of suspended materials (i.e. ~0.1 - 20 g m^{-3}).

Figure 8 shows the relationship between the subsurface volume reflectances R_{VR} and R_{VG} as determined from MOMS in the red and green wavelengths, respectively. Since the two volume reflectances display such a high linear relationship

$$R_{VG} = 0.045 + 2.38\ R_{VR} \qquad (30)$$

with $r = 0.95$ and $\sigma = \pm 8\%$,

both volume reflectances were considered to be correlatable with the suspended material concentrations.

Figure 9 shows the relationship between the subsurface volume reflectances R_{VR} and R_{VIR} as determined from MOMS in the red and near infra-red wavelengths, respectively. In this instance, however, the linear relationship

$$R_{VIR} = 0.002 + 0.232\ R_{VR} \qquad (31)$$

with $r = 0.86$ and $\sigma = \pm 23\%$

does not suggest as high a degree of correlatability between R_{VIR} and the suspended load.

Figures 10 and 11 illustrate the linear fit of the regressions between the red volume reflectance R_{VR} (0.63 μ - 0.69 μ) as observed

by MOMS and determined from equation (27) and the directly measured concentrations of total seston and suspended sediments, respectively. The data points utilized in these figures represent one point per water sampling station. The volume reflectance value was determined as the average volume reflectance resulting from the continuous recording of the upwelling radiance while the research vessel was on station. Figures 12 and 13 illustrate the corresponding linear regressions for the green volume reflectance, R_{VG} (0.52 μ - 0.60 μ), while Figures 14 and 15 illustrate the corresponding linear regressions for the volume reflectance in the near infra-red R_{VIR} (0.8 μ - 1.1 μ).

The linear regressions obtained from Figures 10 through 15 are as follows:

For seston concentration S (g m^{-3}) versus red R_{VR}, green R_{VG} and infra-red R_{VIR} volume reflectances

$$S = -1.72 + 218\ R_{VR} \qquad (32)$$

with correlation coefficient r = 0.86 and standard deviation of the errors σ=±28%

$$S = -5.23 + 87.0\ R_{VG} \qquad (33)$$

with r = 0.85 and σ = ±28%

$$S = -0.03 + 596\ R_{VIR} \qquad (34)$$

with r = 0.63 and σ = ±43%

For suspended sediment concentrations SS (g m^{-3}) versus R_{VR}, R_{VG}, and R_{VIR}

$$SS = -1.73 + 183\ R_{VR} \tag{35}$$

with $r = 0.86$ and $\sigma = \pm 28\%$

$$SS = -4.73 + 73.6\ R_{VG} \tag{36}$$

with $r = 0.86$ and $\sigma = \pm 28\%$

$$SS = -0.17 + 489\ R_{VIR} \tag{37}$$

with $r = 0.62$ and $\sigma = \pm 46\%$

Clearly, the linear relationships involving the visible wavelength volume reflectances and the seston and sediment concentrations display comparable reliability, a reliability which is substantially greater than those of the corresponding relationships involving the near infra-red volume reflectance.

However, as previously discussed, the theoretically anticipated relationships involving the spectral volume reflectance and suspended mineral concentrations in natural waters are decidedly non-linear over substantial ranges of suspended mineral concentration. Distinct asymptotic behaviour is observed at both very small and relatively large concentrations of suspended load. For the range of suspended load encountered in this Lake St. Clair study (2.5 - 20 g m^{-3}), these non-linear asymptotic relationships were approximated by an exponential curve of the form

$$\text{concentration} = A\, e^{kR_{VS}(0)} \tag{38}$$

where A and k are both constants.

Figures 16 through 21 illustrate the counterparts of Figures 10 through 15, respectively. In these figures, however, the best fit exponential curve [equation (38)] rather than the best-fit linear curve, is fitted to the data points.

These best-fit exponential regressions obtained from Figures 16 through 21 are:

$$S = 1.43\, e^{10.5R_{VG}} \tag{39}$$

with $r = 0.86$ and $\sigma = \pm 22\%$

$$S = 2.22\, e^{25.8\, R_{VR}} \tag{40}$$

with $r = 0.85$ and σ $\pm 24\%$

$$S = 2.62\, e^{73.3\, R_{VIR}} \tag{41}$$

with $r = 0.65$ and σ $\pm 36\%$

$$SS = 1.06\, e^{11.0\, R_{VG}} \tag{42}$$

with $r = 0.87$ and σ $\pm 22\%$

$$SS = 1.69\, e^{26.9\, R_{VR}} \tag{43}$$

with $r = 0.86$ and σ $\pm 24\%$

$$SS = 2.06\, e^{74.1\, R_{VIR}} \tag{44}$$

with $r = 0.64$ and σ $\pm 38\%$

Once again the relationships involving the visible volume reflectances and the suspended materials display comparable and greater reliabilities than do their infra-red counterparts. However, the reliabilities of the exponential relationships eclipse the reliabiities of the linear relationships for all three spectral volume reflectance values. Consequently, the remainder of this communication will restrict its consideration to the exponential relationships involving the visible green R_{VG} and visible red R_{VR} volume reflectances [equations (39), (40), (42), and (43)]. While these exponential relationships are considered operational equations for this Lake St. Clair study, it must be noted that extrapolation of such exponential empirical relationships to include volume reflectance values substantially below or above the range of values encountered in the regression analysis is fraught with uncertainty. For example, equations (39) and (40) suggest that values of seston concentrations below 1.43 g m^{-3} and 2.22 g m^{-3} cannot be detected by R_{VG} and R_{VR}, respectively. Similarly, equations (42) and (43) suggest that values of suspended sediment concentrations below 1.06 g m^{-3} and 1.69 g m^{-3} cannot be detected by R_{VG} and R_{VR}, respectively. Obviously, should very small or very large volume reflectance values be observed, there are mathematical extrapolation techniques which may be applied to modify the mid-range exponential curves arising from the regression exercise. However, since the range of volume reflectances observed in this investigation were well within the range of values depicted in Figures 10 to 21, no such extrapolation techniques were deemed necessary in this work.

INTERCOMPARISON OF REMOTE AND IN SITU OPTICAL MEASUREMENTS PERFORMED ON AND IN LAKE ST. CLAIR

The combined processes of scattering and absorption control the manner in which impinging radiation propagates through a natural water mass. The nature and magnitude of the scattering and absorption processes depend, in turn, upon the nature and concentrations of the suspended and dissolved organic and inorganic materials distributed within the water column, as well as upon the nature and radiance distribution of the impinging radiation.

The intensive field study of Lake St. Clair in 1985 afforded the opportunity to evaluate these optical processes from vantage positions both beneath and above the air/water interface. Lake St. Clair, being a rather shallow water body (depths seldom exceeding ~6 metres), performs a receptacle/flow-through function for the transport of water from the Upper Great Lakes to the Lower Great Lakes. As a consequence, the optical scattering and absorption processes occurring within the Lake St. Clair waters are largely under control of either suspended or bottom-resuspended sediment particulates. The optical impact of these suspended particulates were observed by subsurface measurements of transmission (which yielded determinations of the total attenuation coefficient c(z)) and above-surface measurements of upwelling spectral radiance recorded by the ship-mounted MOMS (which through the methodologies discussed earlier in this report yielded determinations of the subsurface spectral volume reflectance $R_{VS}(0)$).

As an estimate of the degree of cohesiveness combining these independent optical measurements, it was decided to utilize the MOMS and in situ optical data set from the September 1985 surveys to estimate the optical relationships arising from the in situ optical surveillance surveys throughout the 1985 field season. The method employed was as follows: The subsurface volume reflectances derived from MOMS were regressed with the corresponding directly measured seston and suspended sediment concentrations. The attenuation coefficients as determined by in situ transmissometry were then regressed against the subsurface volume reflectances simultaneously obtained by MOMS. The subsurface volume reflectance was then mathematically eliminated from the set of regression equations and the resulting mathematical expression relating attenuation coefficient and suspended load was compared to the regression obtained from the lake surveillance surveys. The relationships between the red subsurface volume reflectance R_{VR} determined from MOMS and the directly measured seston S and suspended sediment SS concentrations are given in equations (33) and (36), respectively. The relationship between the attenuation coefficient c appropriate to the upper 1 metre of water column and the red subsurface volume reflectance R_{VR} was determined to be

$$c = -1.13 + 157\ R_{VR} \qquad (45)$$

Eliminating R_{VR} from the pair of equations [(33) and (45)] and [(36) and (45)], respectively, yield:

$$S = -0.15 + 1.39\ c \tag{46}$$

and $$SS = -0.40 + 1.17\ c \tag{47}$$

The regression correlations between c(z) and each of S(z) and SS(z) observed during the lake surveillance surveys are given in equations (3) and (4), respectively. Over the range of measured attenuation coefficients the differences between equations (46) and (3) and between equations (47) and (4) were <3%, indicating a high degree of cohesiveness between the two independent sets of optical measurements.

SESTON AND SUSPENDED SEDIMENT CONCENTRATIONS IN LAKE ST. CLAIR

From the continuously recorded values of L_{Up}, H_{HIGH}, and H_{LOW}, equation (23) was used to calculate the corresponding spectral values of the subsurface volume reflectance R_V. Equation (27) was then used to normalize these R_V values to a fixed solar zenith angle of 0°, viz, $R_{VS}(0)$. These $R_{VS}(0)$ spectral values were then used in conjunction with equations (39), (40), (42) and (43) to provide remote estimates of the seston and suspended sediment concentrations along the ship track in Lake St. Clair.

Figure 22 illustrates the results of the ship transect of September 13, 1985. Herein are plotted the calculated seston concentrations in g m^{-3} (based on 30 sec averages of the continuously determinable values of $R_{VS}(0)$ in the visible red MOMS channel

(0.63 μ - 0.69 μ) as a function of both time and ship location. The continuous curve represents the predicted values of seston concentrations based on the continuous operation of MOMS. The non-continuous horizontal bars represent the values of seston concentrations determined from the water samples collected at the fixed monitoring stations, the length of the horizontal bar representing the time spent at the station. One very apparent discrepancy between these two sets of seston values, particularly for the first five station visitations, is the consistently higher values of seston recorded by the in situ water sampling techniques as compared to the values remotely determined by MOMS. One very probable cause for this is bottom sediment-resuspension generated by the ship's backwash. The occurrence of such sediment-resuspension is further suggested by the very noticeable increased "spiking" in the seston concentrations determined remotely by MOMS at the station locations. A possible explanation for MOMS consistently recording values of seston concentrations lower than those recorded via direct water collection may be found in the fact that MOMS is boom-mounted in advance of the ship while the direct sampling occurs off mid-ship. Clearly, therefore, while both MOMS and direct sampling techniques are considering water masses which are representative of the aquatic region under study, the particular water masses to which each is directly exposed are not identical, particularly when shallow waters are significantly agitated by the measurement process. It is further seen from Figure 22 that as the ship transect progressed from the very shallow (2-3 metres) near-shore stations to the deeper (5-6 metres)

off-shore stations, the discrepancies between MOMS and direct sampling decreased in magnitude.

While Figure 22 represents a transect from the eastern shore of Lake St. Clair to roughly mid lake, Figure 23 represents a cross-lake transect from west to east taken on September 14, 1985, again using the upwelling red radiance (0.63 μ - 0.69 μ) continuously recorded by MOMS. In this instance considerably less discrepancies are apparent between the on-station direct sampling and the on-station remote sampling, suggesting that the problem of bottom-resuspension was under considerably more control than it was the day before. However, here too, it is seen that the "spiking" is more prominent in the shallower near shore aquatic regimes than in the offshore waters.

It is also clearly seen, however, that both the east and west nearshore regions are characterized by significantly higher concentrations of total suspended material than the slightly deeper mid-lake regions. Also very noticeable in the cross-lake transect is the increased seston concentrations between sampling stations 66 to 69. This corresonds to the location and immediate environs of the artificially deepened shipping channel through Lake St. Clair. The increased suspended material both predicted by MOMS and measured by direct sampling are undoubtedly a consequence of bottom resuspension initiated by ship traffic.

Figure 24 illustrates the estimates of seston (on an expanded time scale covering about 30 minutes) resulting from red volume reflectance measurements performed on September 19, 1985. Much of the

displayed time period of Figure 24 was spent with the ship on-station, and one very obvious feature of this figure is the high degree of stability displayed by MOMS during these periods. This is in direct contrast to the somewhat sporadic nature of the MOMS seston estimates of Figures 22 and 23. A careful perusal of Figures 22 and 23, however, reveal that the major discontinuities in the MOMS curves occur when the vessel is both arriving at and departing from the sampling station. Clearly, if future work of this type is to be considered, more serious thought must be assigned to field logistics and in situ data gathering procedures, to ensure that the measurement processes do not adversely impact the scientific purpose of the mission. In defense of the field data-gathering procedures, however, it should be pointed out that the investigations of September 13 and 14 formed part of a collaborative venture with another research team that utilized aircraft overflights in conjunction with the ship transects. Attempting a coordinated data collection activity involving observation platforms of dissimilar speeds and data collecting properties places an inordinate onus on the slower moving vehicle, and can therefore result in one or both of the vehicles violating the systematic controls to which they would normally adhere.

Figures 25, 26, and 27 are the green band (0.52 μ - 0.60 μ) equivalents of the red band Figures 22, 23, and 24. Once again the remotely determined MOMS estimates of seston concentrations are displayed as the continuous curve while the discontinuous horizontal bars represent the seston concentrations measured by direct sampling at the fixed monitoring stations.

Figure 28 illustrates the calculated and directly sampled suspended sediment concentrations in g m^{-3} for the ship transect of September 13, 1985 (based on 30 sec averages of the continuously determinable values of $R_{VS}(0)$ in the visible red MOMS channel (0.63 μ - 0.69 μ) as a function of both time and ship location in an identical manner to the seston concentration curve of Figure 22. The similarities between Figures 28 and 22 are immediately apparent, and the possible impact of ship-induced bottom resuspension is once again a most noticeable feature of Figure 28.

Figures 29 and 30 illustrate the remote (and directly sampled) suspended sediment concentrations for the ship transect of September 14 and September 19, 1985, respectively, utilizing the MOMS visible red channel volume reflectance data as the source of remote estimation of suspended sediment concentrations.

Figures 31, 32, and 33 are the visible green channel (0.52 μ - 0.60 μ) equivalents of the red channel curves of Figures 28, 29, and 30. Once again the remotely determined MOMS estimates of suspended sediment concentrations are displayed as the continuous curve while the discontinuous horizontal bars represent the suspended sediment concentrations measured by direct sampling at the fixed monitoring stations.

A very high degree of consistency among the seston and suspended sediment concentrations as determined from the remote measurements of the upwelling radiance by MOMS in the red and the green portions of the visible spectrum, are clearly seen from Figures 22 through 33. Consequently, the discussions applicable to the remote and direct

seston concentration determinations (Figures 22 through 27) are equally applicable to the remote and direct suspended sediment concentration determinations (Figures 28 through 33).

It must be emphasized that the $R_{VS}(0)$ values used in this MOMS project were determined from correlations involving directly measured concentrations in Lake St. Clair. No absorption and/or scattering "cross-sections" were calculated for either the seston or suspended sediment particulates, since the direct sampling techniques (both optical and non-optical) were not as rigorously comprehensive as the large scale activities previously conducted in Lake Ontario (Bukata et al., 1979; 1981a; 1981b; 1981c). It is, however, of interest to compare the results of the current predictions of suspended sediment concentrations over Lake St. Clair (based on correlation techniques) with predictions of suspended sediments (resulting from the use of the optical "cross-sections") determined from the earlier Lake Ontario work. It must be realized, of course, that departures from identical predictive values encountered in such a comparison, are not necessarily due solely to the differences in both the nature and rigor of the techniques employed in the water quality modelling activities, but could very possibly be a consequence of dissimilarities between the nature and optical behaviour of the classes of particulates indigenous to the two distinct aquatic locations.

Figure 34 presents a comparison between the suspended sediment concentration values as a function of $R_{VS}(0)$ for the visible red (0.63 μ - 0.69 μ) MOMS channel as predicted from the current Lake St. Clair study (Curve A) and the former Lake Ontario study (Curve B).

Curve B was calculated on the assumption that the Lake Ontario chlorophyll a concentrations were included in the range 0-10 mg m^{-3} and the dissolved organic carbon concentrations were included in the range 1-4 g m^{-3}. No per se Lake St. Clair chlorophyll or dissolved organic carbon concentrations were considered in the calculation of Curve A, which is just a direct consequence of the exponential equation (43). While Curves A and B display an obvious similarity in basic shape, they also display an obvious dissimilarity. In addition to Curve B (Lake Ontario) initiating its low sediment concentration onset at a larger $R_{VS}(0)$ red value, the Lake Ontario curve is characterized by a faster rising slope than is Curve A (Lake St. Clair). The two curves intersect and reverse the sign of the relative difference between their predictions at intermediate to large values of encountered suspended sediment concentrations. Despite the differences in the methodologies utilized in these two optical environmental studies, the differences in the predictive capabilities of these two models is indicative of the difficulties which must be anticipated when environmental models appropriate to one set of environmental parameters are considered for application to another possibly dissimilar set of environmental parameters.

ACKNOWLEDGEMENTS

The optical activities discussed in this communication were performed in tandem with an intensive limnological/remote sensing study of Lake St. Clair. The seston and suspended mineral

concentrations were obtained as an integral part of this intensive study and their presence is a direct consequence of the organizational skills and logistical expertise of the multi-faceted team responsible for this Lake St. Clair study. It is a pleasure to acknowledge our gratitude to the key roles played by F.M. Boyce, P.F. Hamblin, J.A. Bull, T.J. Simons, D.G. Robertson, C.R. Murthy, Y. Marmoush, I. Stepien, and the crews of the C.S.S. Limnos and C.S.S. Advent.

REFERENCES

Bukata, R.P., J.H. Jerome, J.E. Bruton, and S.C. Jain. 1979. Determination of Inherent Optical Properties of Lake Ontario Coastal Waters. Appl. Opt. 18, 3926-3932.

Bukata, R.P., J.H. Jerome, J.E. Bruton, S.C. Jain and H.H. Zwick. 1981a. Optical Water Quality Model of Lake Ontario. 1. Determination of the Optical Cross Sections of Organic and Inorganic Particulates in Lake Ontario. Appl. Opt. 20, 1696-1703.

Bukata, R.P., J.H. Jerome, J.E. Bruton, S.C. Jain and H.H. Zwick. 1981b. Optical Water Quality Model of Lake Ontario. 2. Determination of Chlorophyll *a* and Suspended Mineral Concentrations of Natural Waters from Submersible and Low Altitute Optical Sensors. Appl. Opt. 20, 1704-1714.

Bukata, R.P., J.H. Jerome, and J.E. Bruton. 1981c. Validation of a Five-Component Optical Model for Estimating Chlorophyll a and Suspended Mineral Concentrations in Lake Ontario. Appl. Opt. 20, 3472-3474.

Bukata, R.P., J.H. Jerome, and J.E. Bruton. 1985a. Direct Optical Measurements of the Laurentian Great Lakes. Part II: An Optical Atlas. NWRI Report No. 85-25, 170 pp.

Bukata, R.P, J.E. Bruton, and J.H. Jerome. 1985b. Application of Direct Measurements of Optical Parameters to the Estimation of Lake Water Quality Indicators. Env. Can. IWD Scientific Series No. 140, 35 pp.

Cox, C. and W. Munk. 1955. Some Problems in Optical Oceanography. J. Mar. Res. 14, 63-78.

Duntley, S.Q., R.W. Austin, W.H. Wilson, C.F. Edgerton, and S.E. Moran. 1974. Ocean Color Analysis. Scripps Institution of Oceanography, San Diego. SIO Ref. 74-10, 67 pp.

Gordon, J.I. 1969. Directional Radiance (Luminance) of the Sea Surface. Scripps Institution of Oceanography, San Diego. SIO Ref 69-20.

Jerlov, N.G. 1984. Marine Optics, Elsevier, New York, 231 pp.

Maul, G.A. 1985. Introduction to Satellite Oceanography, Martinus Nijhoff Publishers, Dordrecht/Boston/Lancaster, 606 pp.

Payne, R.E. 1972. Albedo of the Sea Surface. J. Atmos. Sci. 29, 959-970.

Watson, A.S., F.E. Roy, and J. Dolanjski. 1982. Handbook Notes for Shipboard Reflectance Radiometer System. Unpublished Manuscript, Engineering Services Section, National Water Research Institute, 44 pp.

FIGURE CAPTIONS

Figure 1: Schematic map of Lake St. Clair illustrating the surveillance sampling stations.

Figure 2: Linear regression between the total seston concentration and the total attenuation coefficient.

Figure 3: Linear regression between the suspended sediment concentration and the total attenuation coefficient.

Figure 4: Schematic representation of the dual radiometer system, MOMS.

Figure 5: Estimated values of Q as a function of solar zenith angle for large backscattering probability (Curve A), low backscattering probability (Curve B), and arithmetic mean (Curve C).

Figure 6: Curve illustrating the impact on $R_{VS}(\theta)$ of varying θ.

Figure 7: Schematic map of Lake St. Clair illustrating ship transects and sampling stations.

Figure 8: Linear regression between the green volume reflectance and the red volume reflectance.

Figure 9: Linear regression between the infra-red volume reflectance and the red volume reflectance.

Figure 10: Linear regression between the red volume reflectance and the total seston concentration.

Figure 11: Linear regression between the red volume reflectance and the suspended sediment concentration.

Figure 12: Linear regression between the green volume reflectance and the total seston concentration.

Figure 13: Linear regression between the green volume reflectance and the suspended sediment concentration.

Figure 14: Linear regression between the infra-red volume reflectance and the total seston concentration.

Figure 15: Linear regression between the infra-red volume reflectance and the suspended sediment concentration.

Figure 16: Exponential regression between the red volume reflectance and the total seston concentration.

Figure 17: Exponential regression between the red volume reflectance and the suspended sediment concentration.

Figure 18: Exponential regression between the green volume reflectance and the total seston concentration.

Figure 19: Exponential regression between the green volume reflectance and the suspended sediment concentration.

Figure 20: Exponential regression between the infra-red volume reflectance and the total seston concentration.

Figure 21: Exponential regression between the infra-red volume reflectance and the suspended sediment concentration.

Figure 22: Total seston concentrations as determined from the visible red channel of MOMS on September 13, 1985 (continuous curve) along with the seston concentrations determined from direct sample collection (non-continuous lines).

Figure 23: Total seston concentrations as determined from the visible red channel of MOMS on September 14, 1985 (continuous curve) along with the seston concentrations determined from direct sample collection (non-continuous lines).

Figure 24: Total seston concentrations as determined from the visible red channel of MOMS on September 19, 1985 (continuous curve) along with the seston concentrations determined from direct sample collection (non-continuous lines).

Figure 25: Total seston concentrations as determined from the visible green channel of MOMS on September 13, 1985 (continuous curve) along with the seston concentrations determined from direct sample collection (non-continuous lines).

Figure 26: Total seston concentrations as determined from the visible green channel of MOMS on September 14, 1985 (continuous curve) along with the seston concentrations determined from direct sample collection (non-continuous lines).

Figure 27: Total seston concentrations as determined from the visible green channel of MOMS on September 19, 1985 (continuous curve) along with the seston concentrations determined from direct sample collection (non-continuous lines).

Figure 28: Suspended sediment concentrations as determined from the visible red channel of MOMS on September 13, 1985 (continuous curve) along with the suspended sediment concentrations determined from direct sample collection (non-continuous lines).

Figure 29: Suspended sediment concentrations as determined from the visible red channel of MOMS on September 14, 1985 (continuous curve) along with the suspended sediment concentrations determined from direct sample collection (non-continuous lines).

Figure 30: Suspended sediment concentrations as determined from the visible red channel of MOMS on September 19, 1985 (continuous curve) along with the suspended sediment concentrations determined from direct sample collection (non-continuous lines).

Figure 31: Suspended sediment concentrations as determined from the visible green channel of MOMS on September 13, 1985 (continuous curve) along with the suspended sediment concentrations determined from direct sample collection (non-continuous lines).

Figure 32: Suspended sediment concentrations as determined from the visible green channel of MOMS on September 14, 1985 (continuous curve) along with the suspended sediment concentrations determined from direct sample collection (non-continuous lines).

Figure 33: Suspended sediment concentrations as determined from the visible green channel of MOMS on September 19, 1985 (continuous curve) along with the suspended sediment concentrations determined from direct sample collection (non-continuous lines).

Figure 34: Suspended sediment concentrations as a function of visible red volume reflectance as predicted from correlations performed in the current Lake St. Clair study (Curve A) and as predicted from "cross sections" determined in Lake Ontario (Curve B).

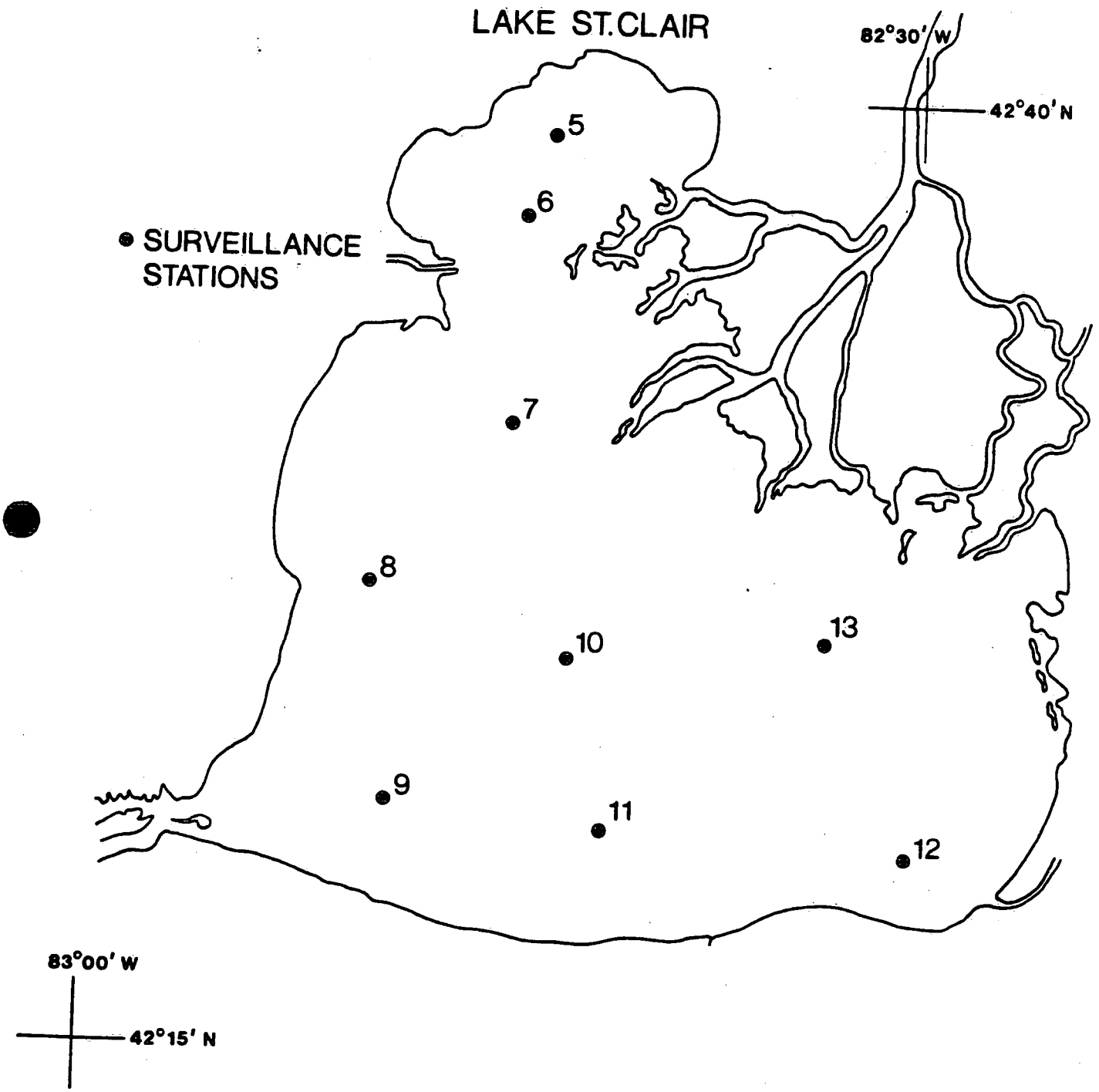
LAKE ST. CLAIR
82°30' W
42°40' N
SURVEILLANCE STATIONS
5
6
7
8
9
10
11
12
13
83°00' W
42°15' N

FIG. 1

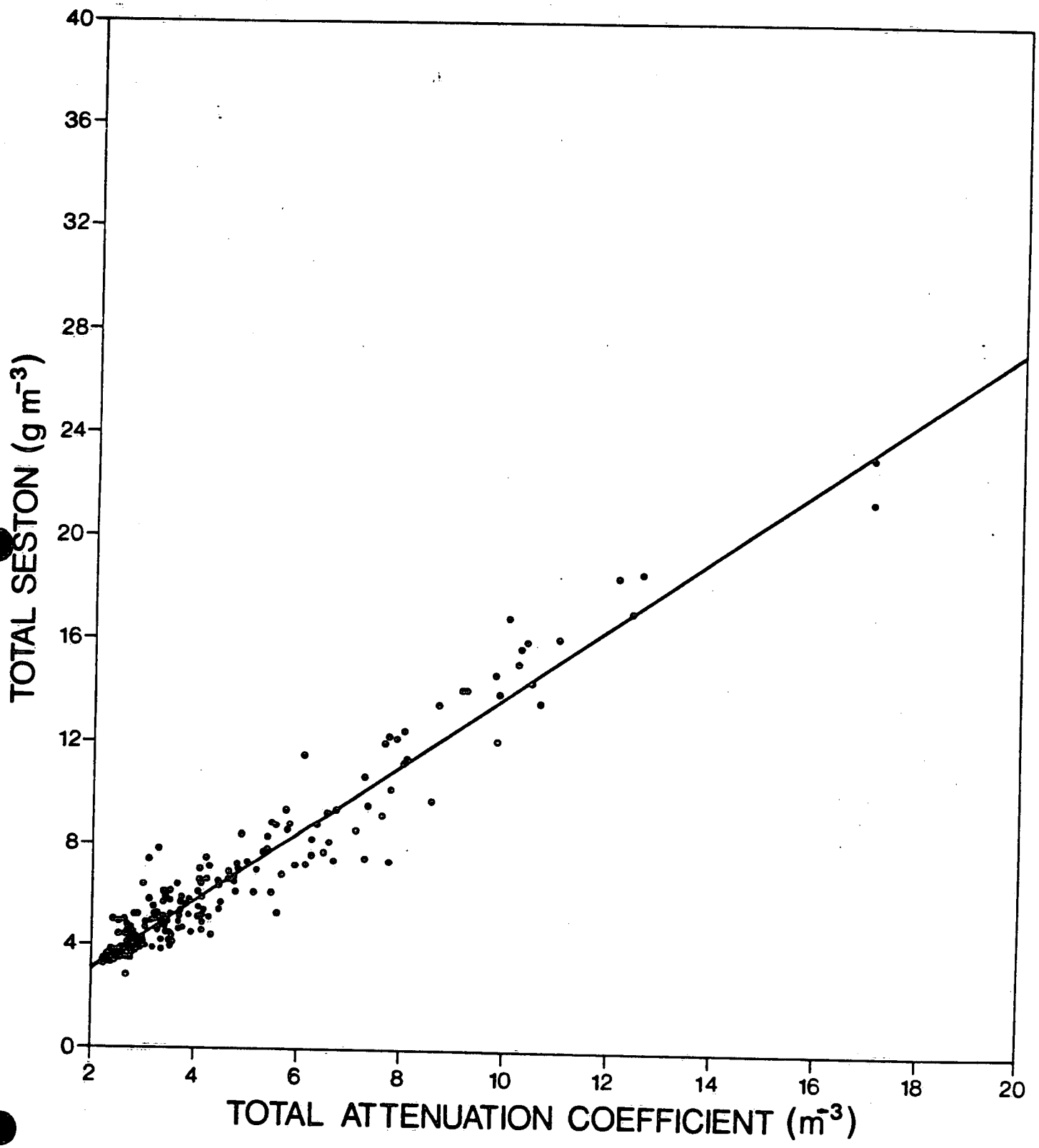
40
36
32
28
24
20
16
12
8
4
0
TOTAL SESTON (g m^{-3})
2
4
6
8
10
12
14
16
18
20
TOTAL ATTENUATION COEFFICIENT (m^{-3})

FIG. 2

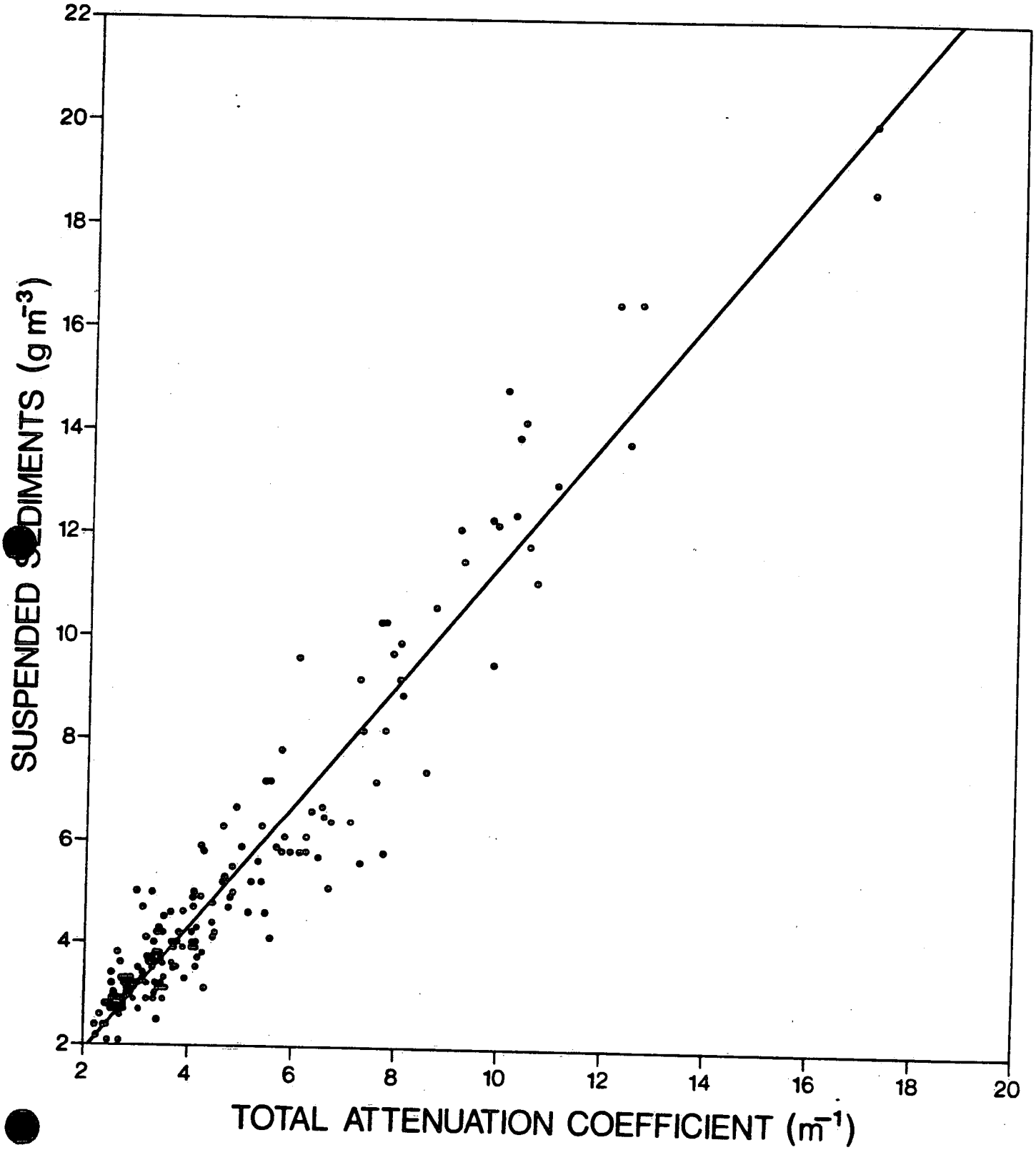
22
20
18
16
14
12
10
8
6
4
2
SUSPENDED SEDIMENTS (g m^{-3})
2
4
6
8
10
12
14
16
18
20
TOTAL ATTENUATION COEFFICIENT (m^{-1})

FIG. 3

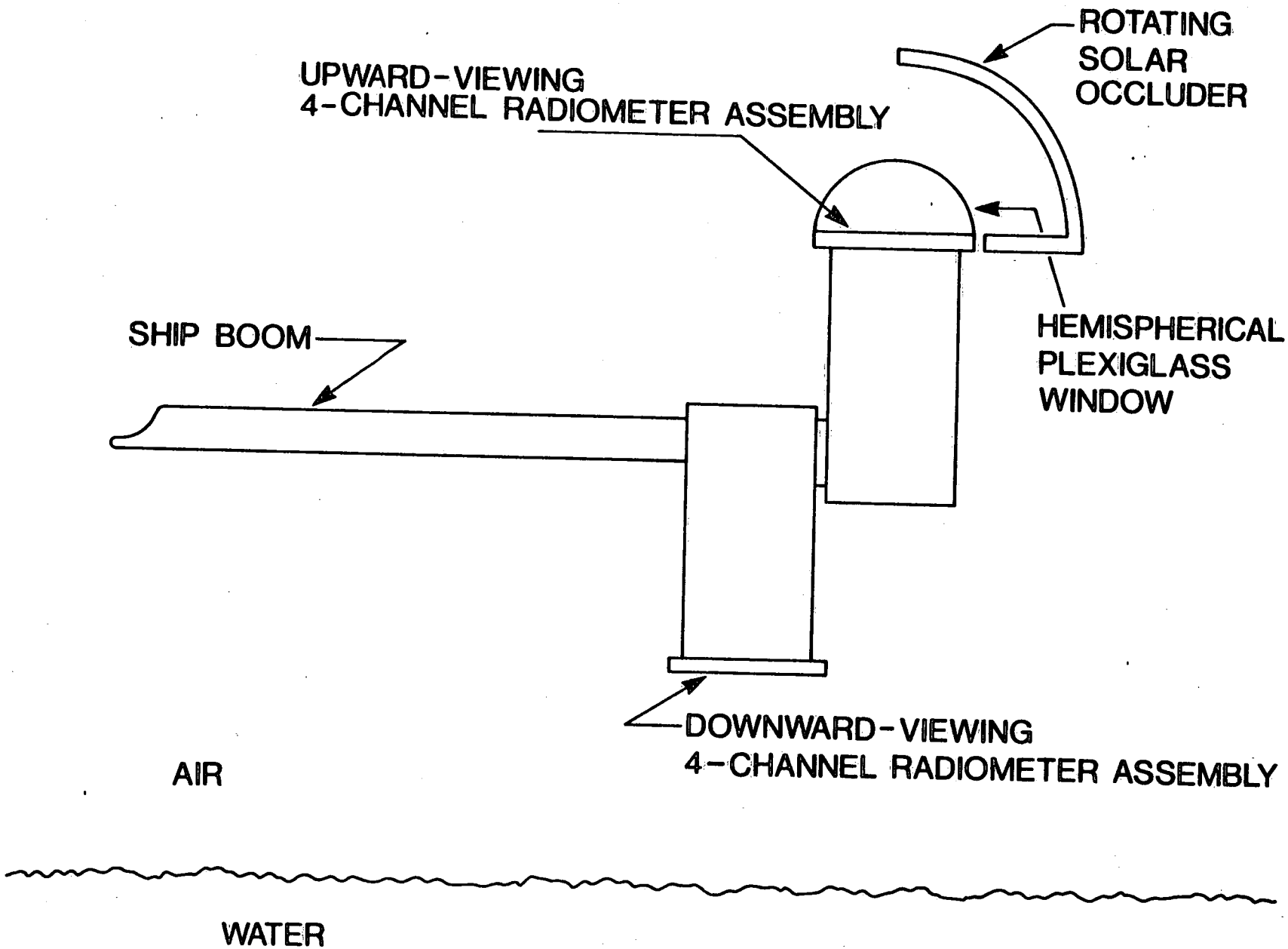
ROTATING
SOLAR
OCCLUDER
UPWARD-VIEWING
4-CHANNEL RADIOMETER ASSEMBLY
SHIP BOOM
HEMISPHERICAL
PLEXIGLASS
WINDOW
DOWNWARD-VIEWING
4-CHANNEL RADIOMETER ASSEMBLY
AIR
WATER

FIG. 4

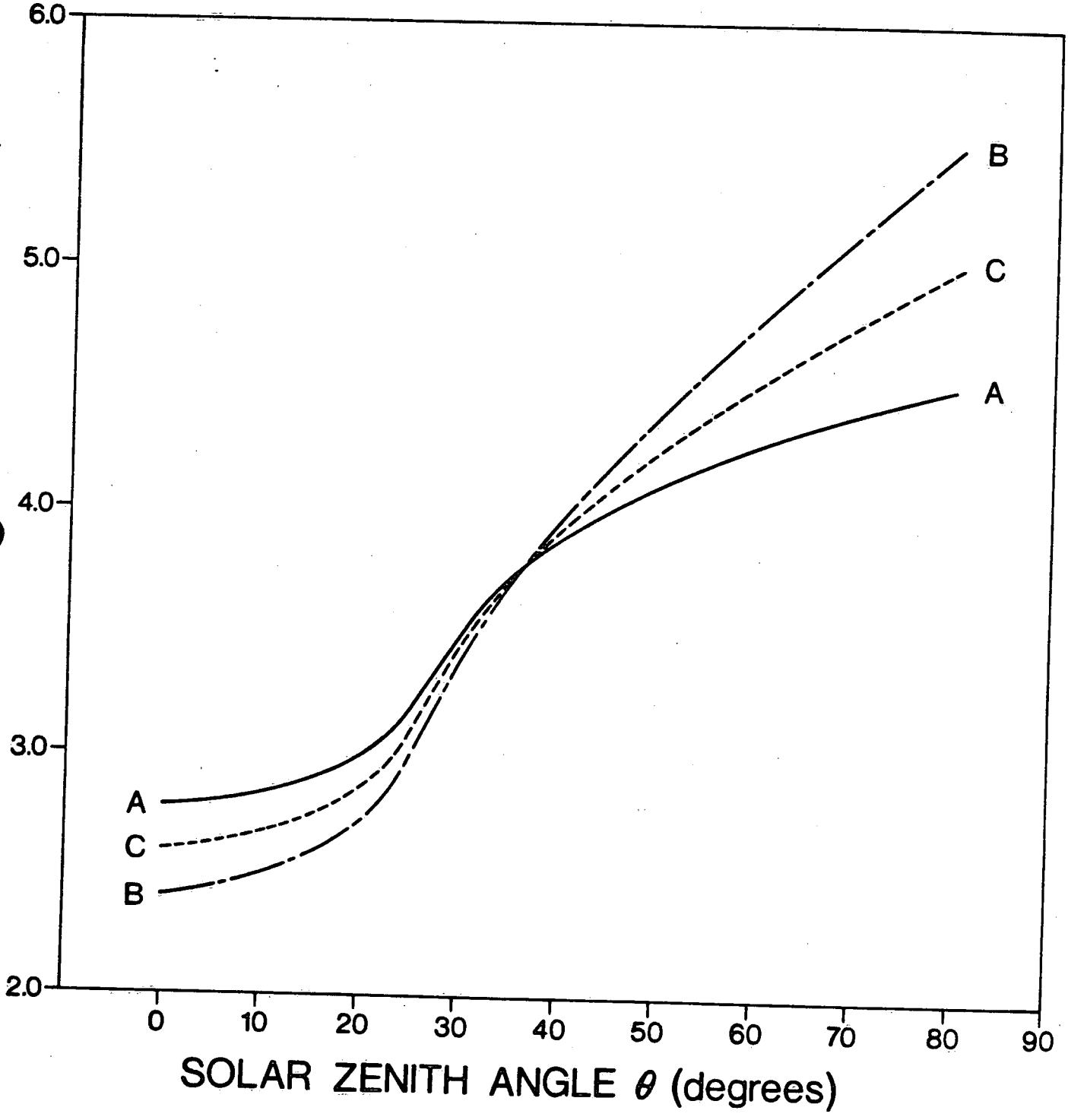
6.0
5.0
4.0
3.0
2.0
Q
B
C
A
A
C
B
0
10
20
30
40
50
60
70
80
90
SOLAR ZENITH ANGLE θ (degrees)

FIG. 5

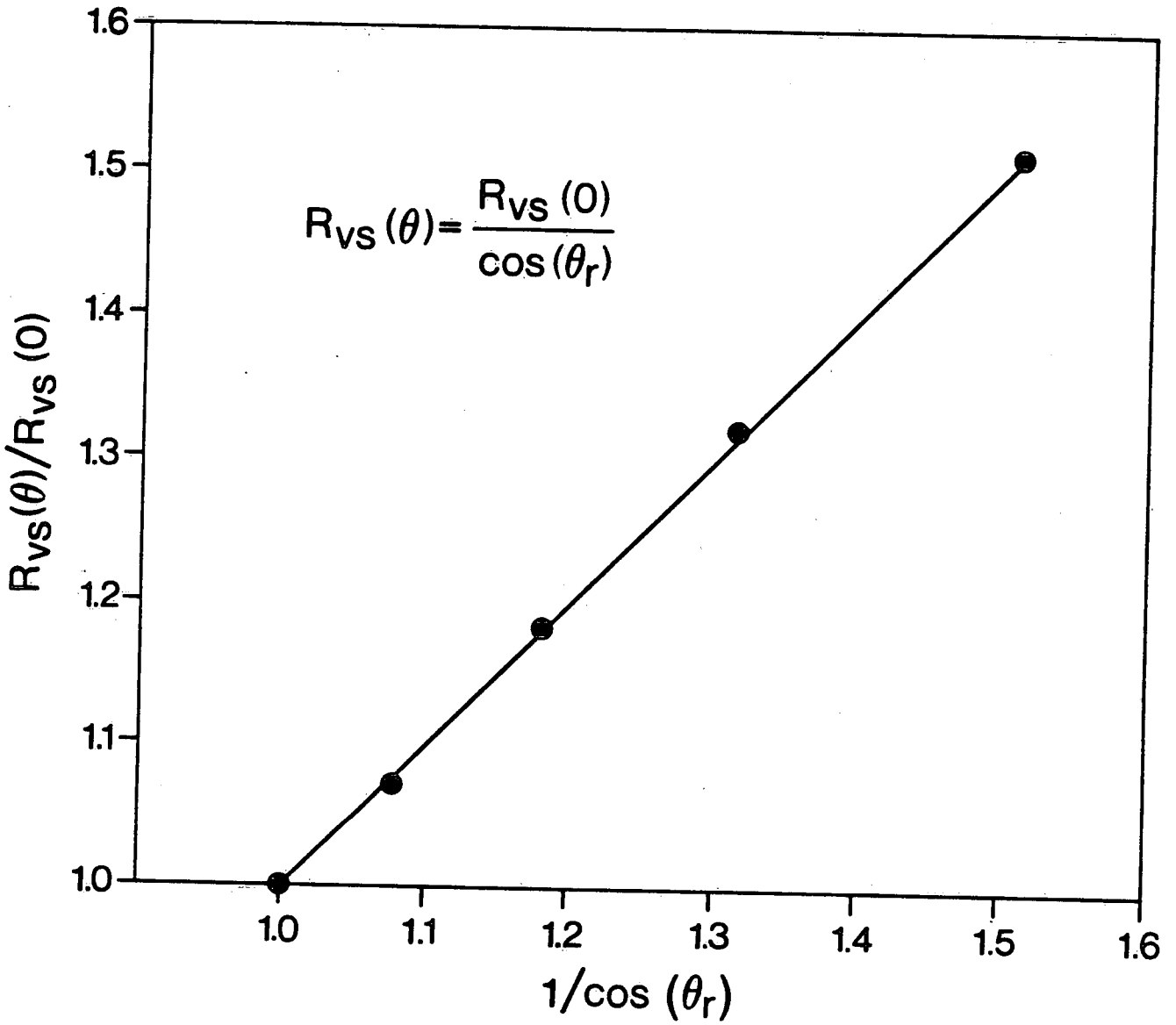
1.6
1.5
1.4
1.3
1.2
1.1
1.0
$R_{VS}(\theta)/R_{VS}(0)$
$R_{VS}(\theta) = \frac{R_{VS}(0)}{\cos(\theta_r)}$
1.0
1.1
1.2
1.3
1.4
1.5
1.6
$1/\cos(\theta_r)$

FIG. 6

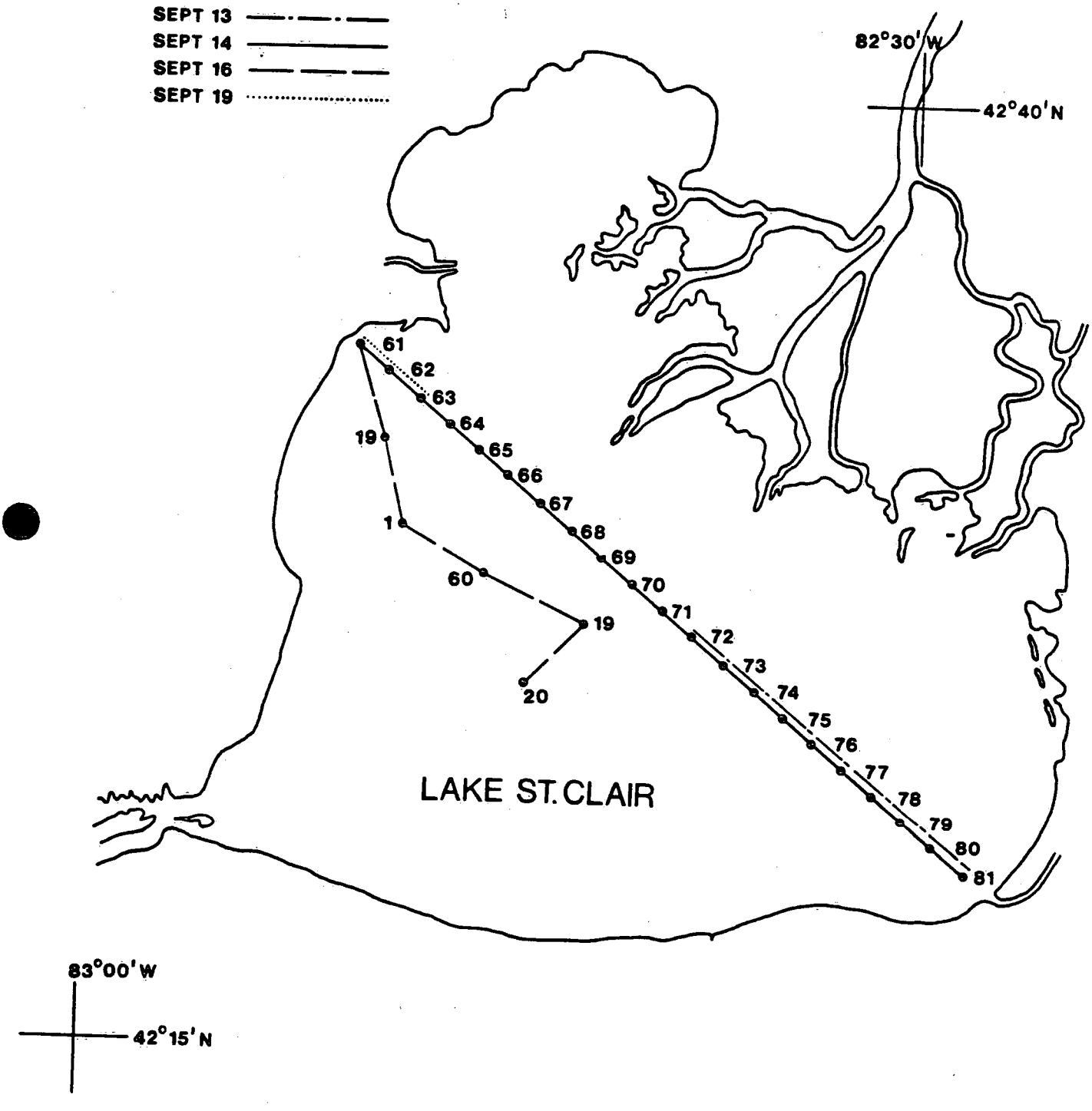
SEPT 13
SEPT 14
SEPT 16
SEPT 19
82°30'W
42°40'N
61
62
63
64
65
66
67
68
69
70
71
72
73
74
75
76
77
78
79
80
81
19
1
60
19
20
LAKE ST. CLAIR
83°00'W
42°15'N

FIG. 7

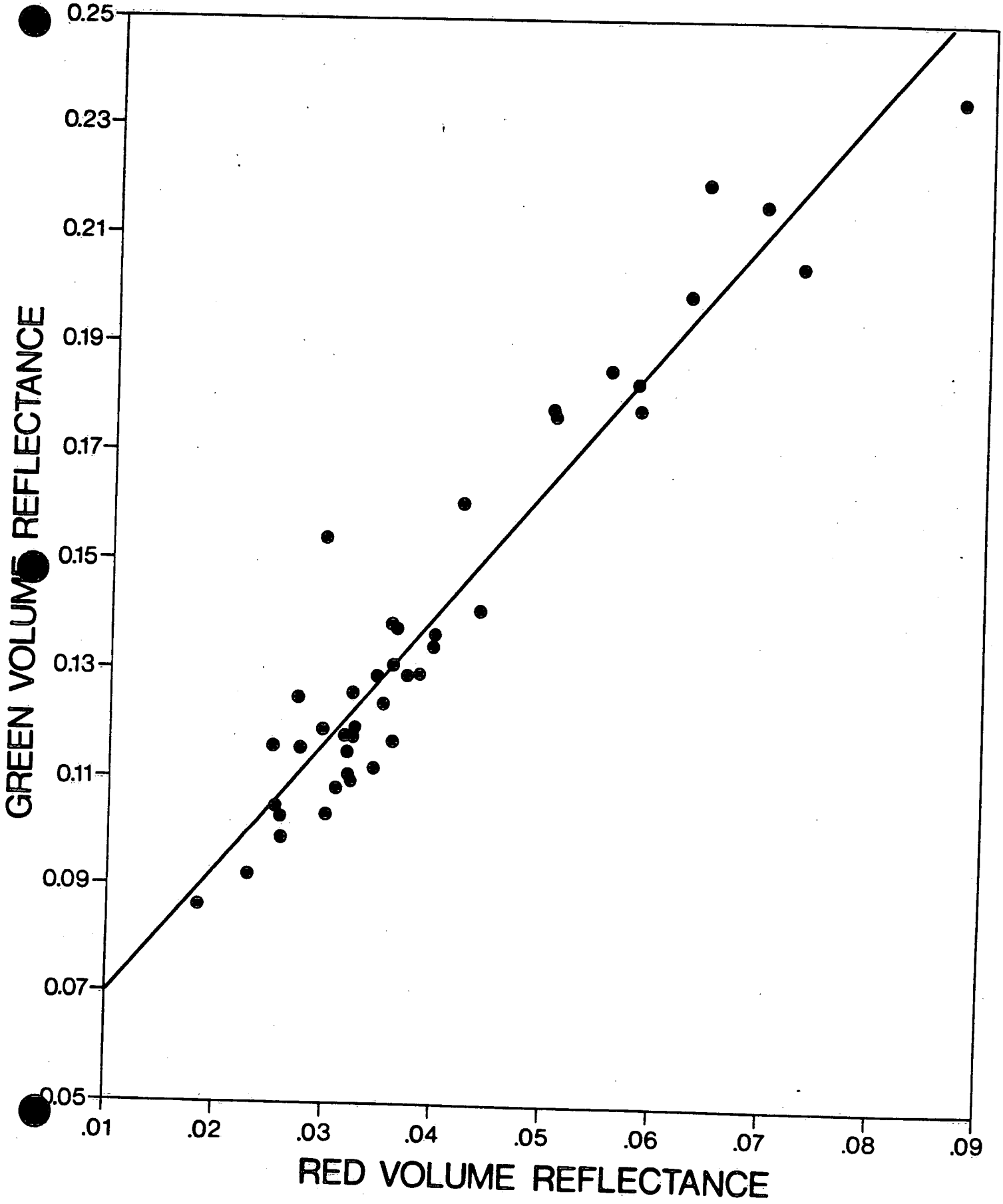
0.25
0.23
0.21
0.19
0.17
0.15
0.13
0.11
0.09
0.07
0.05
GREEN VOLUME REFLECTANCE
.01
.02
.03
.04
.05
.06
.07
.08
.09
RED VOLUME REFLECTANCE

FIG. 8

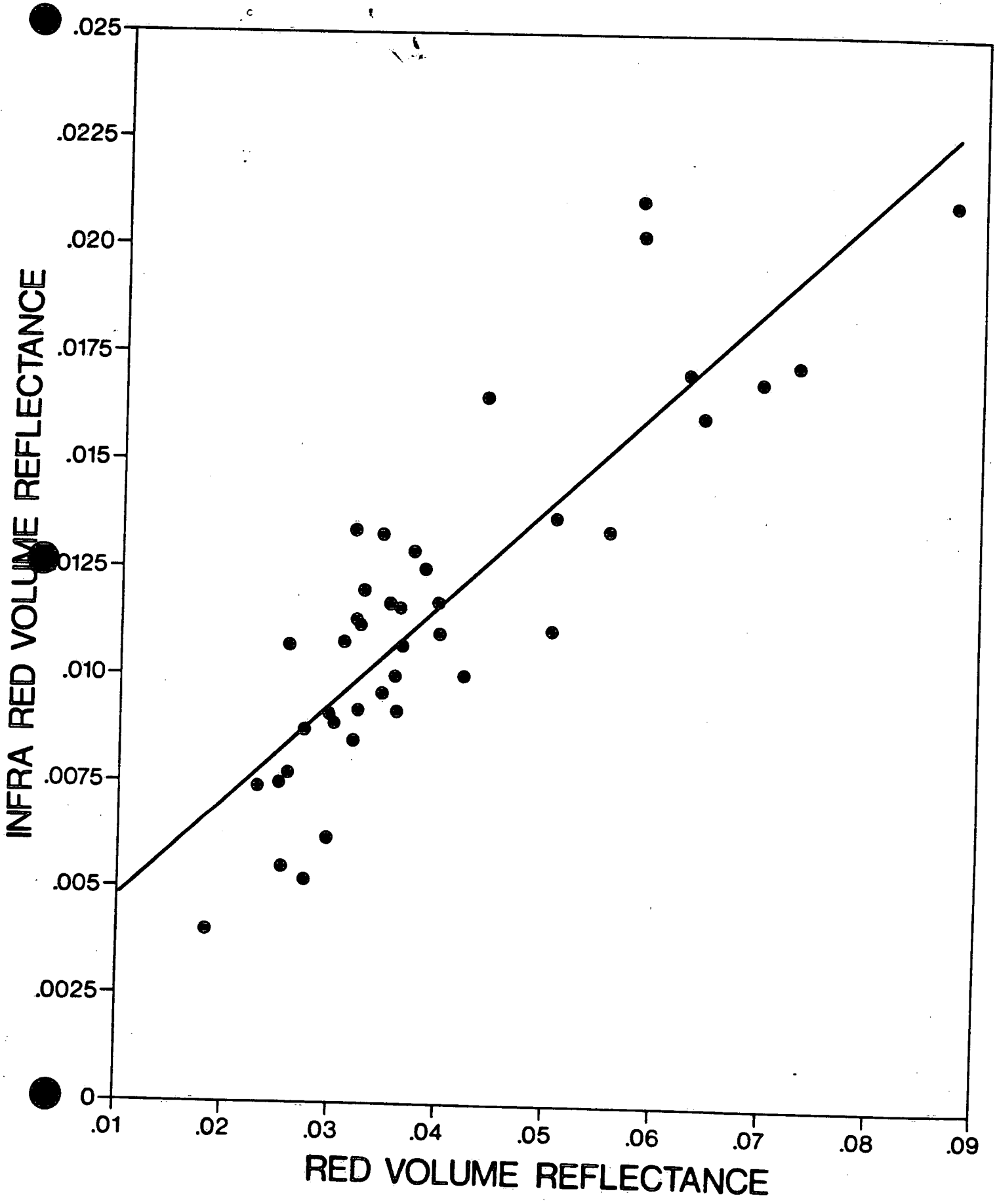
.025
.0225
.020
.0175
.015
.0125
.010
.0075
.005
.0025
0
INFRA RED VOLUME REFLECTANCE
.01
.02
.03
.04
.05
.06
.07
.08
.09
RED VOLUME REFLECTANCE

FIG. 9

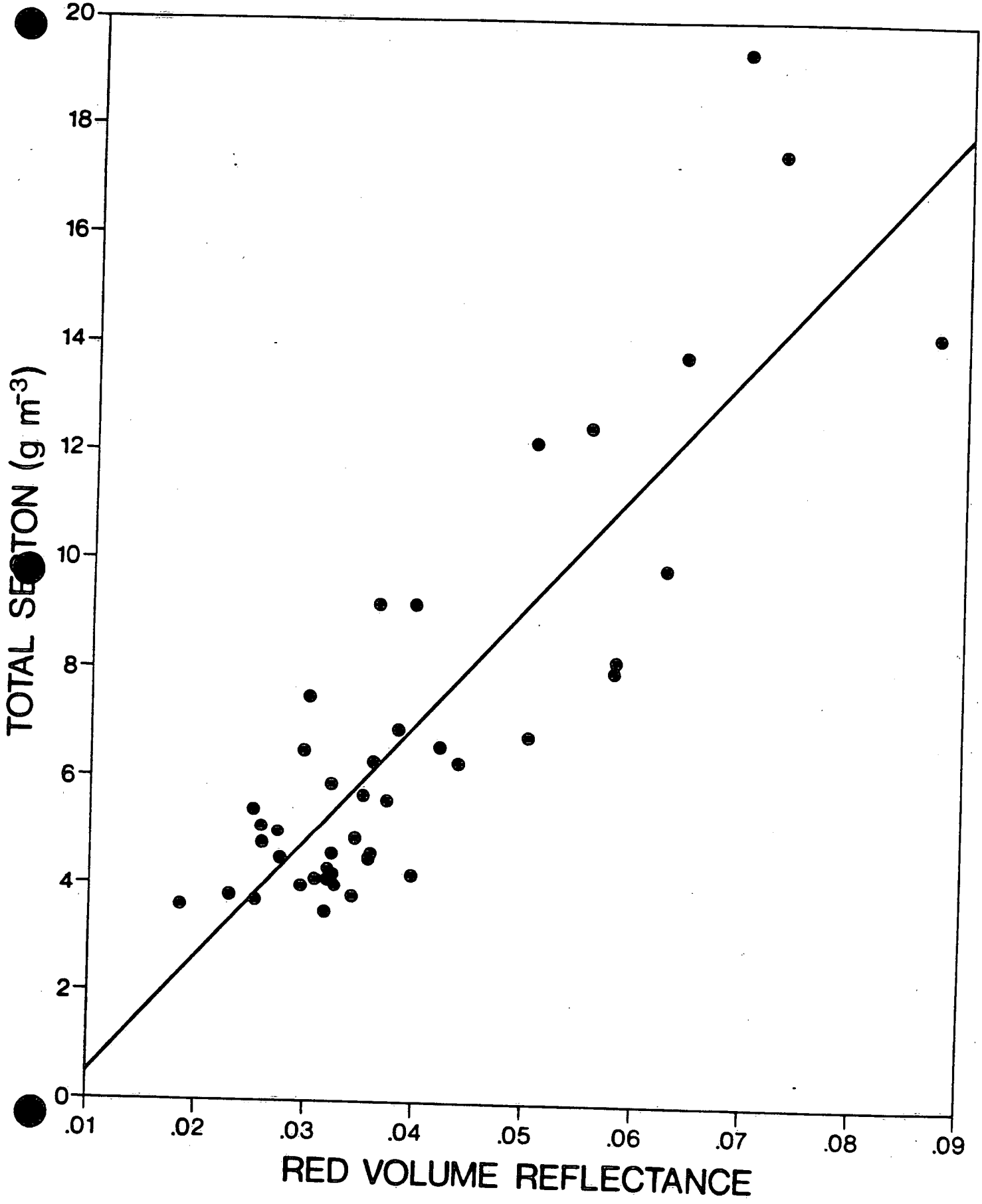
20
18
16
14
12
10
8
6
4
2
0
TOTAL SEDIMENTON (g m-3)
.01
.02
.03
.04
.05
.06
.07
.08
.09
RED VOLUME REFLECTANCE

FIG. 10

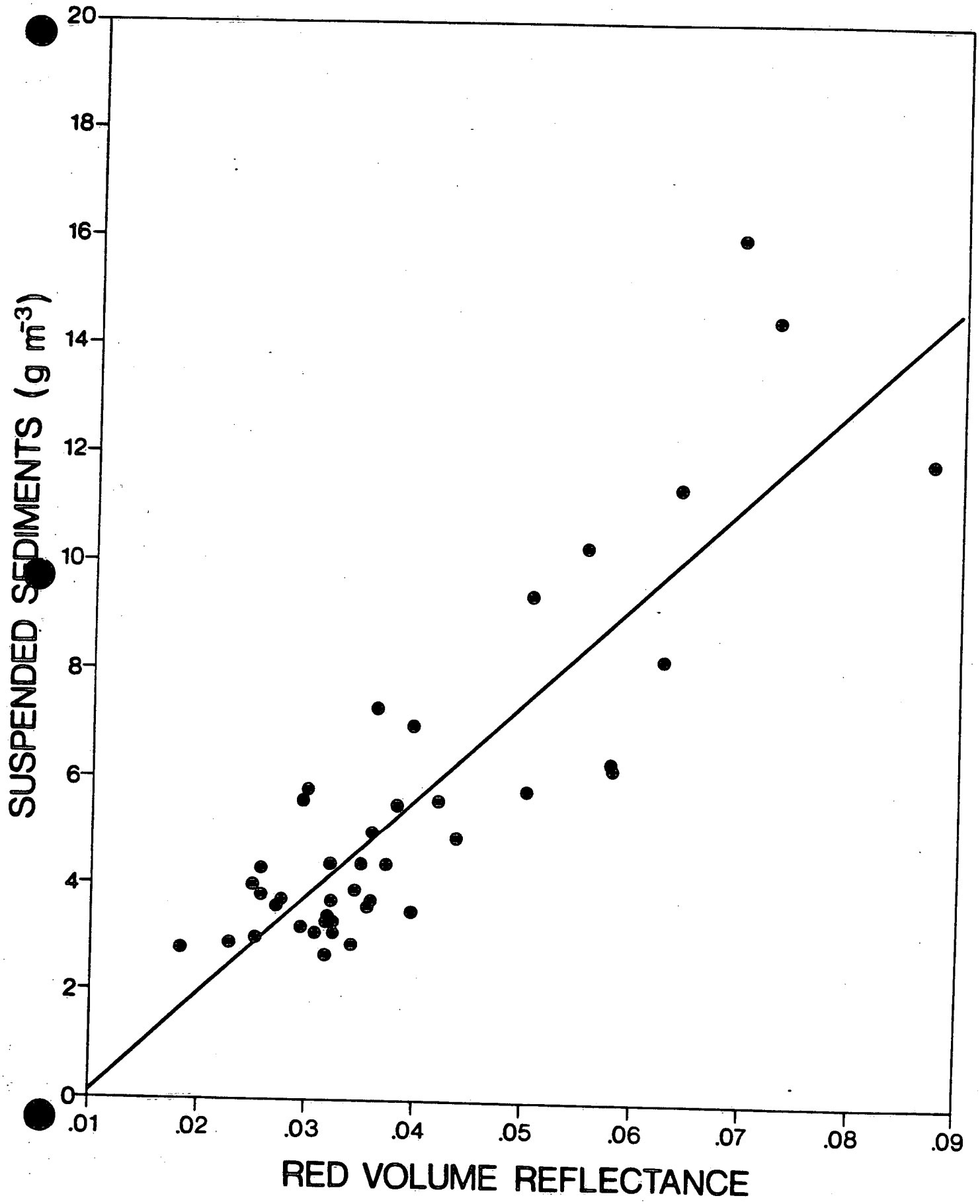
20
18
16
14
12
10
8
6
4
2
0
SUSPENDED SEDIMENTS (g m^{-3})
.01
.02
.03
.04
.05
.06
.07
.08
.09
RED VOLUME REFLECTANCE

FIG. 11

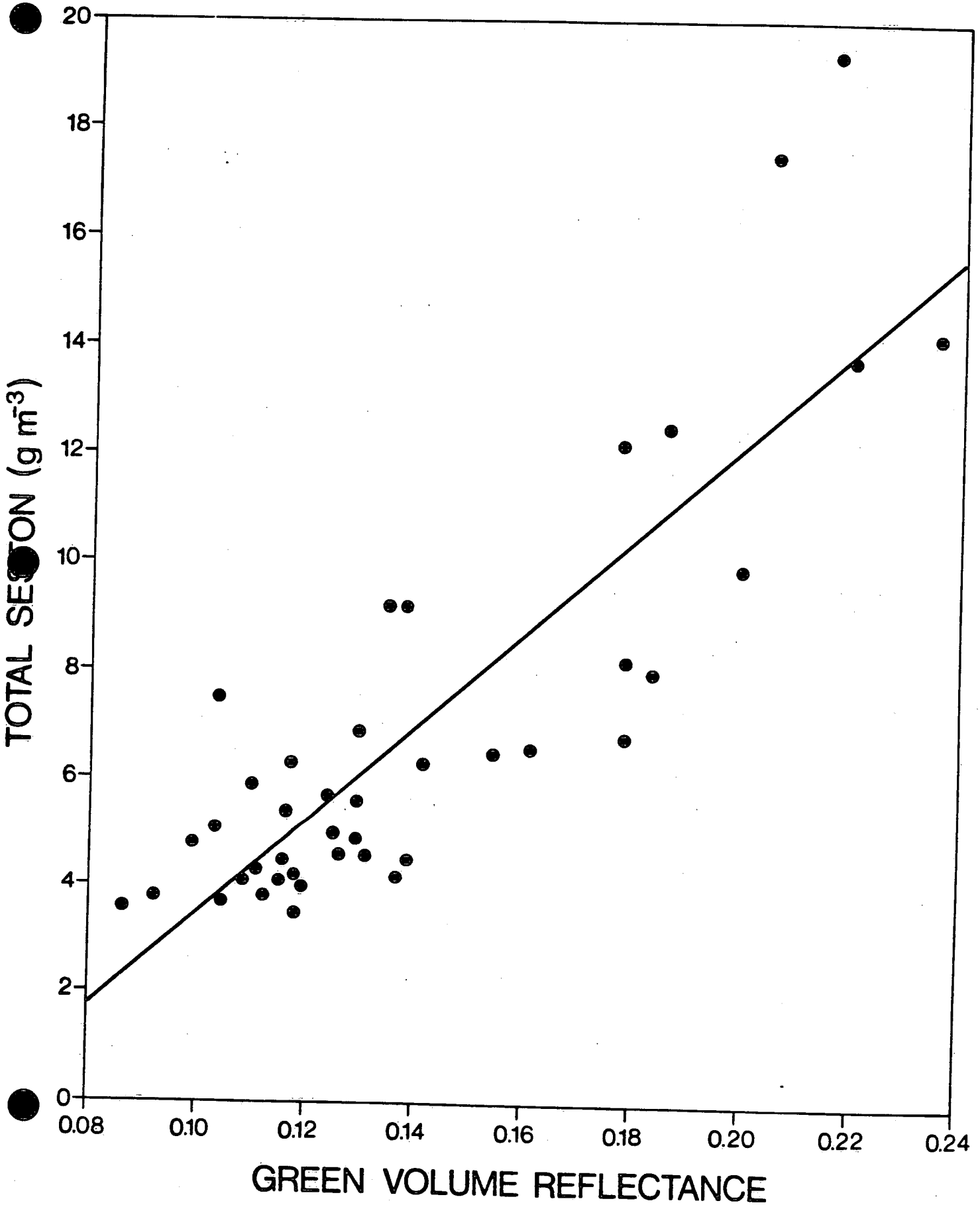
20
18
16
14
12
10
8
6
4
2
0
TOTAL SE TON (g m-3)
0.08
0.10
0.12
0.14
0.16
0.18
0.20
0.22
0.24
GREEN VOLUME REFLECTANCE

FIG. 12

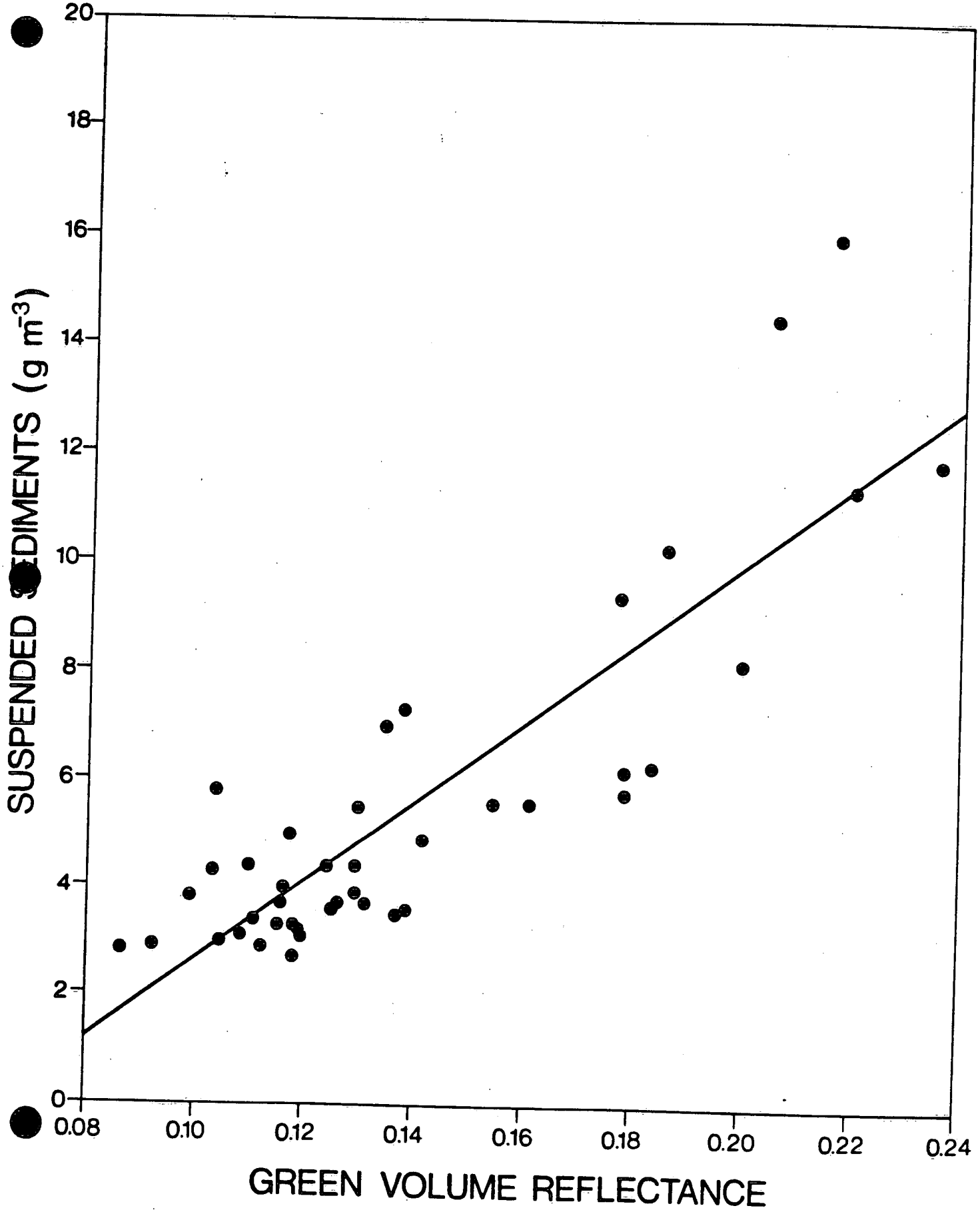
20
18
16
14
12
10
8
6
4
2
0
SUSPENDED SEDIMENTS (g m-3)
0.08
0.10
0.12
0.14
0.16
0.18
0.20
0.22
0.24
GREEN VOLUME REFLECTANCE

FIG. 13

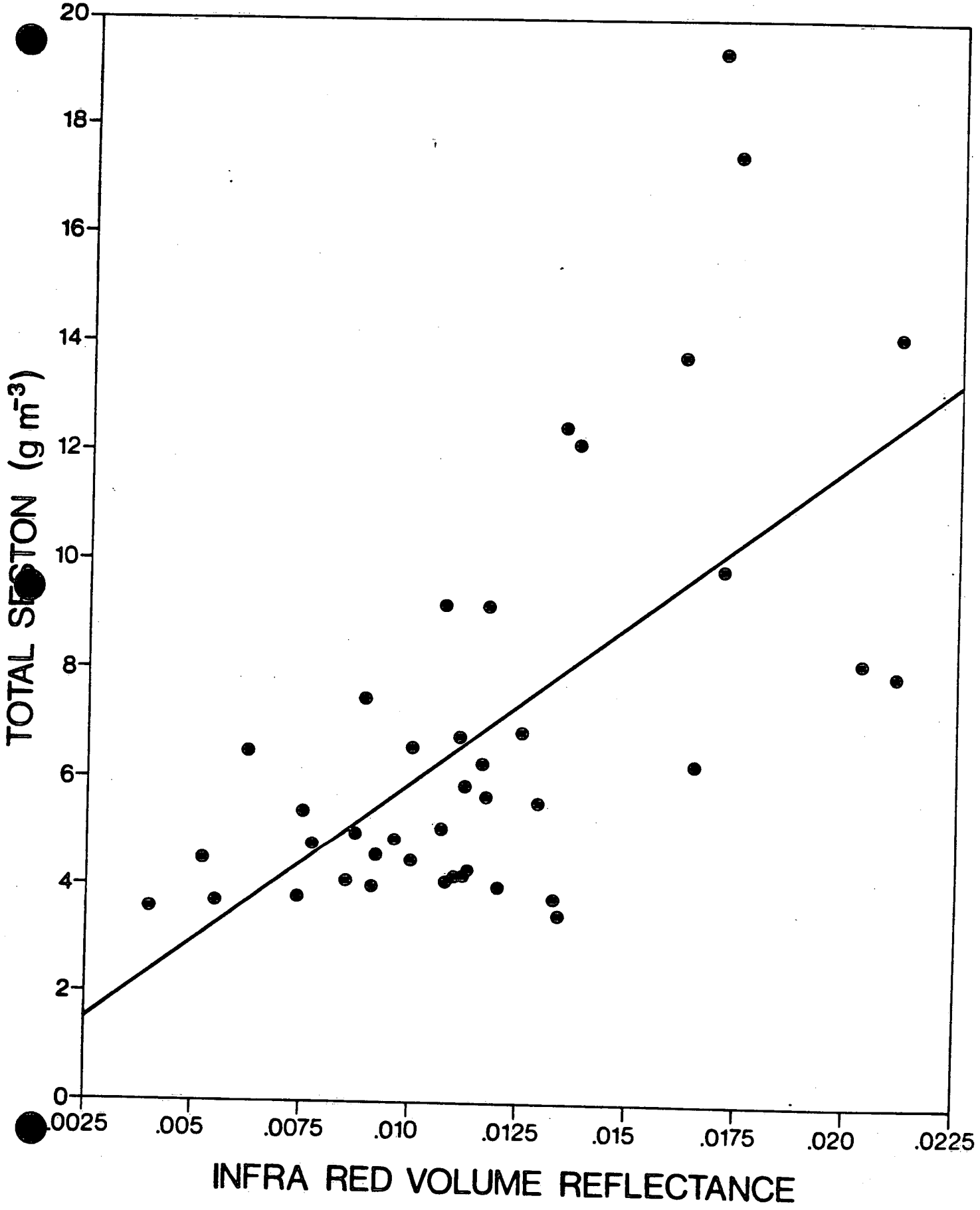
20
18
16
14
12
10
8
6
4
2
0
TOTAL SESTON (g m^{-3})
.0025
.005
.0075
.010
.0125
.015
.0175
.020
.0225
INFRA RED VOLUME REFLECTANCE

FIG. 14

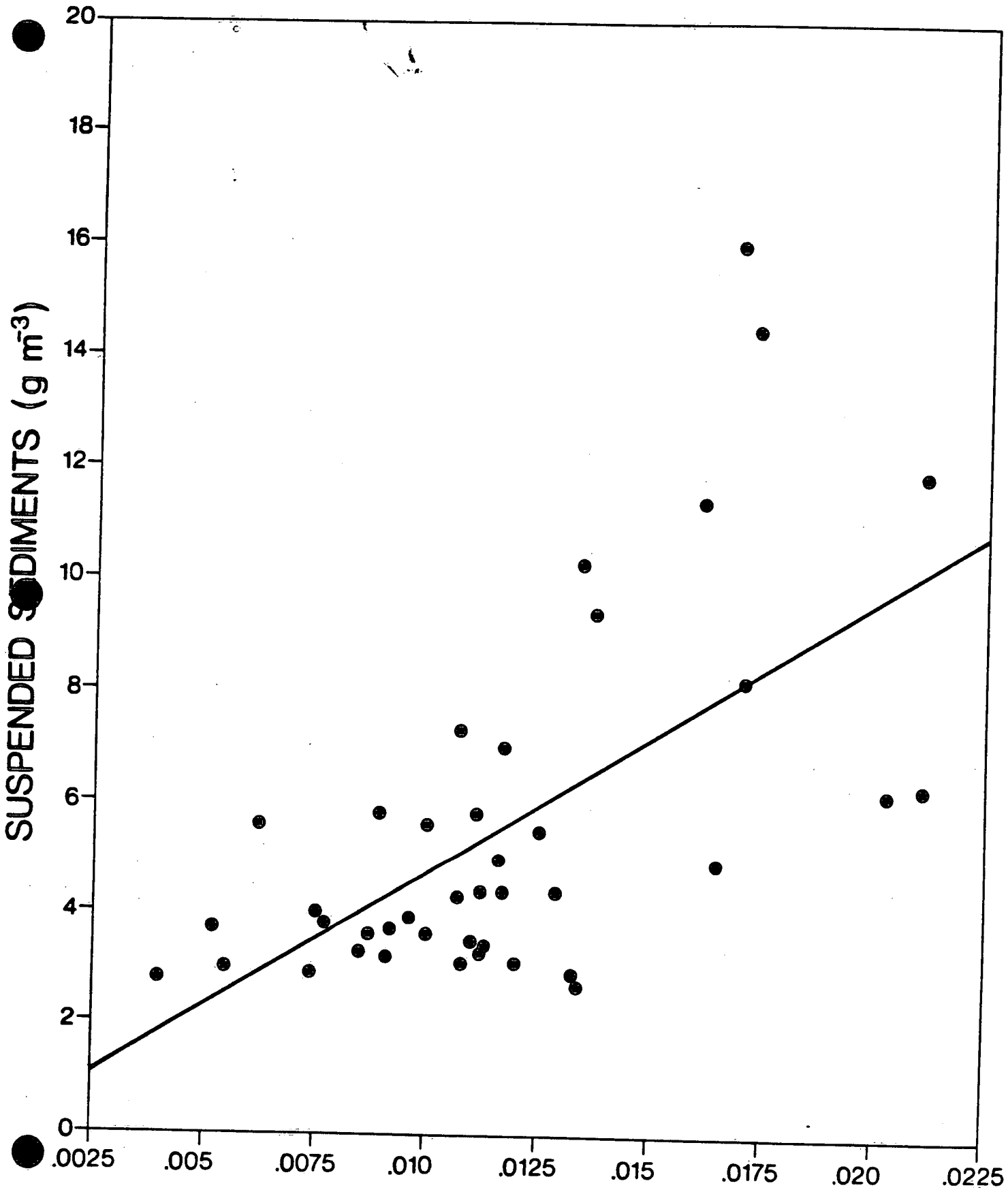
20
18
16
14
12
10
8
6
4
2
0
SUSPENDED SEDIMENTS (g m^{-3})
.0025
.005
.0075
.010
.0125
.015
.0175
.020
.0225
INFRA RED VOLUME REFLECTANCE

FIG. 15

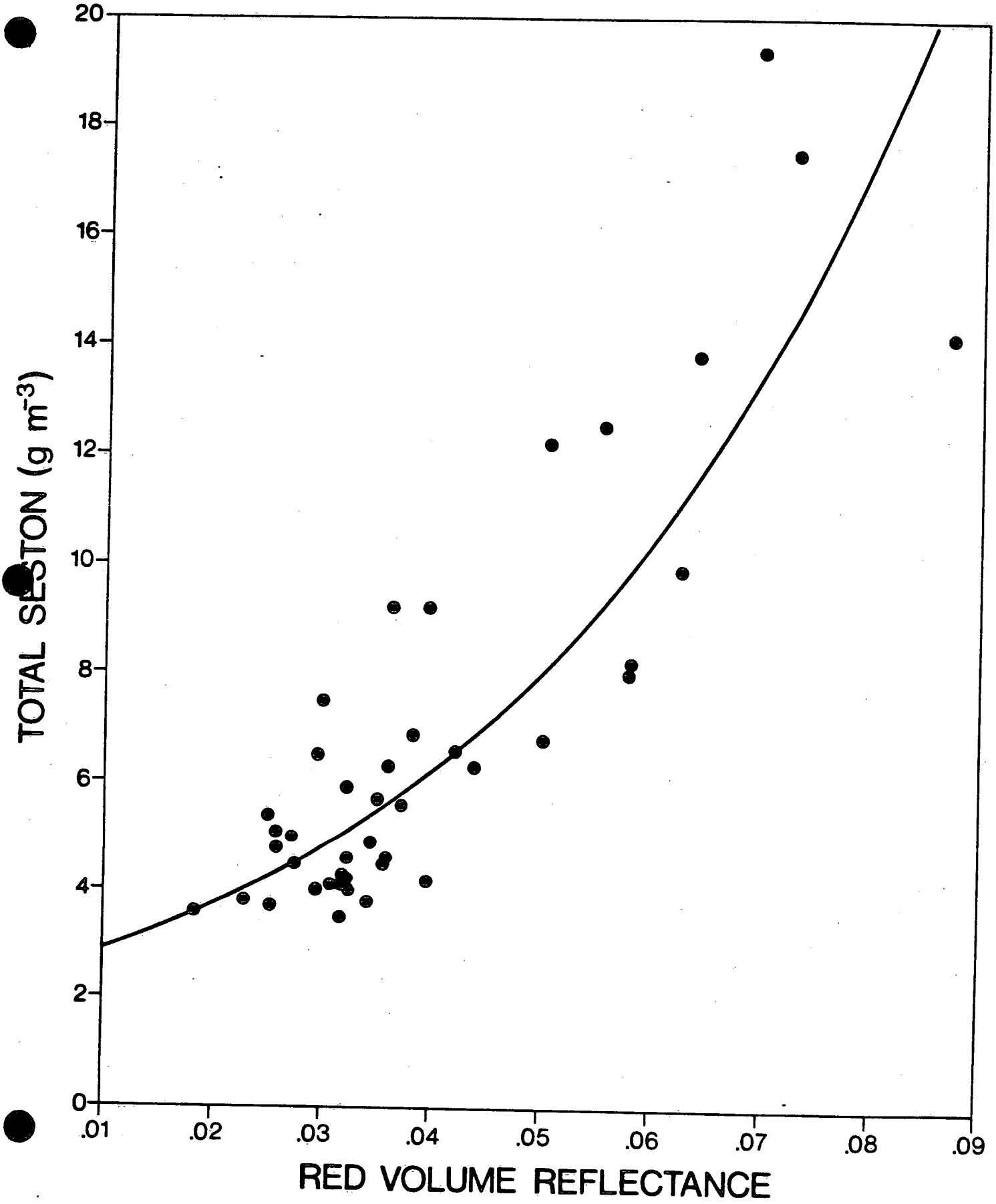
20
18
16
14
12
10
8
6
4
2
0
TOTAL SESTON (g m^{-3})
.01
.02
.03
.04
.05
.06
.07
.08
.09
RED VOLUME REFLECTANCE

FIG. 16

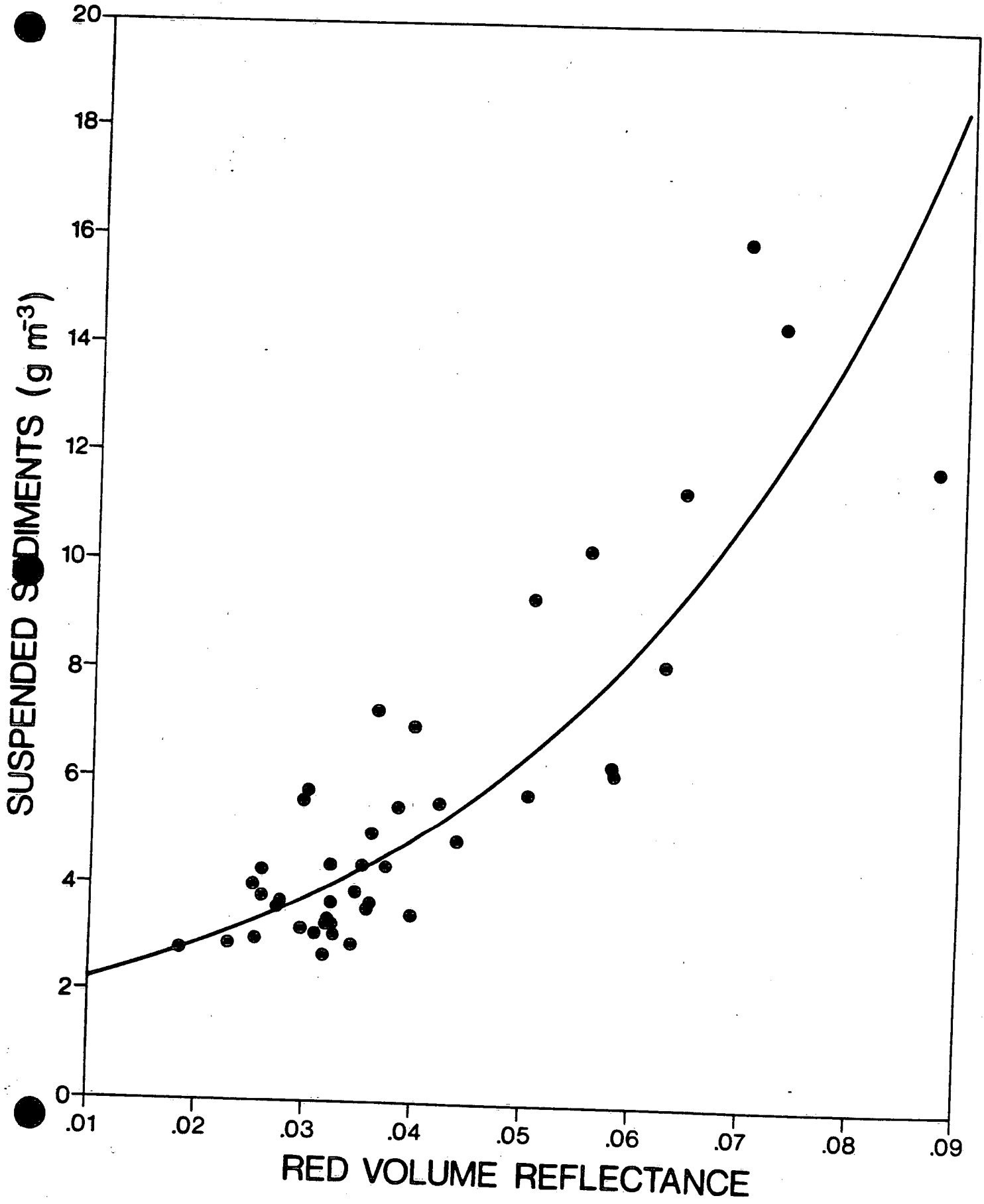
20
18
16
14
12
10
8
6
4
2
0
SUSPENDED SEDIMENTS (g m-3)
.01
.02
.03
.04
.05
.06
.07
.08
.09
RED VOLUME REFLECTANCE

FIG. 17

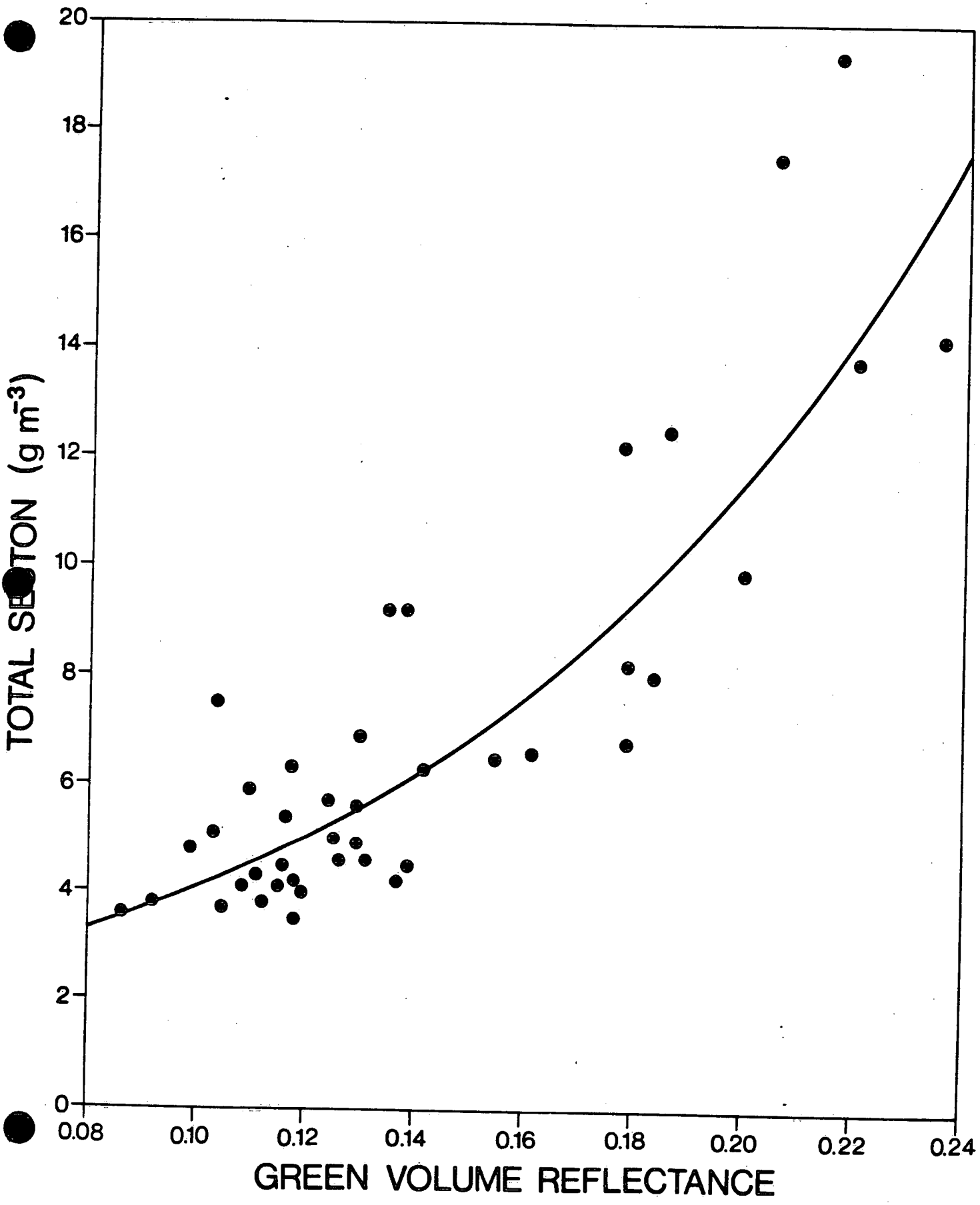
20
18
16
14
12
10
8
6
4
2
0
TOTAL SESTON (g m^{-3})
0.08
0.10
0.12
0.14
0.16
0.18
0.20
0.22
0.24
GREEN VOLUME REFLECTANCE

FIG. 18

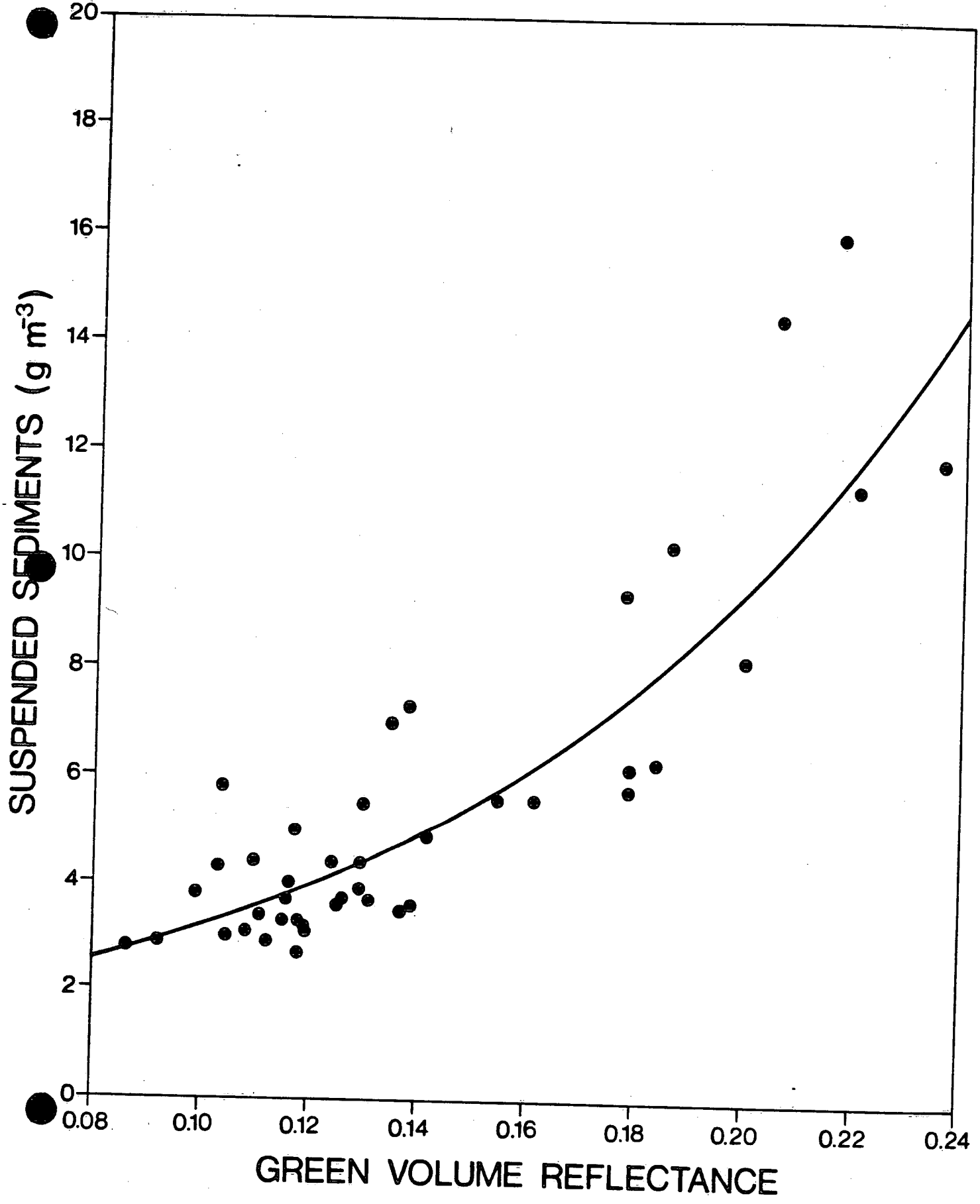
SUSPENDED SEDIMENTS (g m^{-3})
20
18
16
14
12
10
8
6
4
2
0
0.08
0.10
0.12
0.14
0.16
0.18
0.20
0.22
0.24
GREEN VOLUME REFLECTANCE

FIG. 19

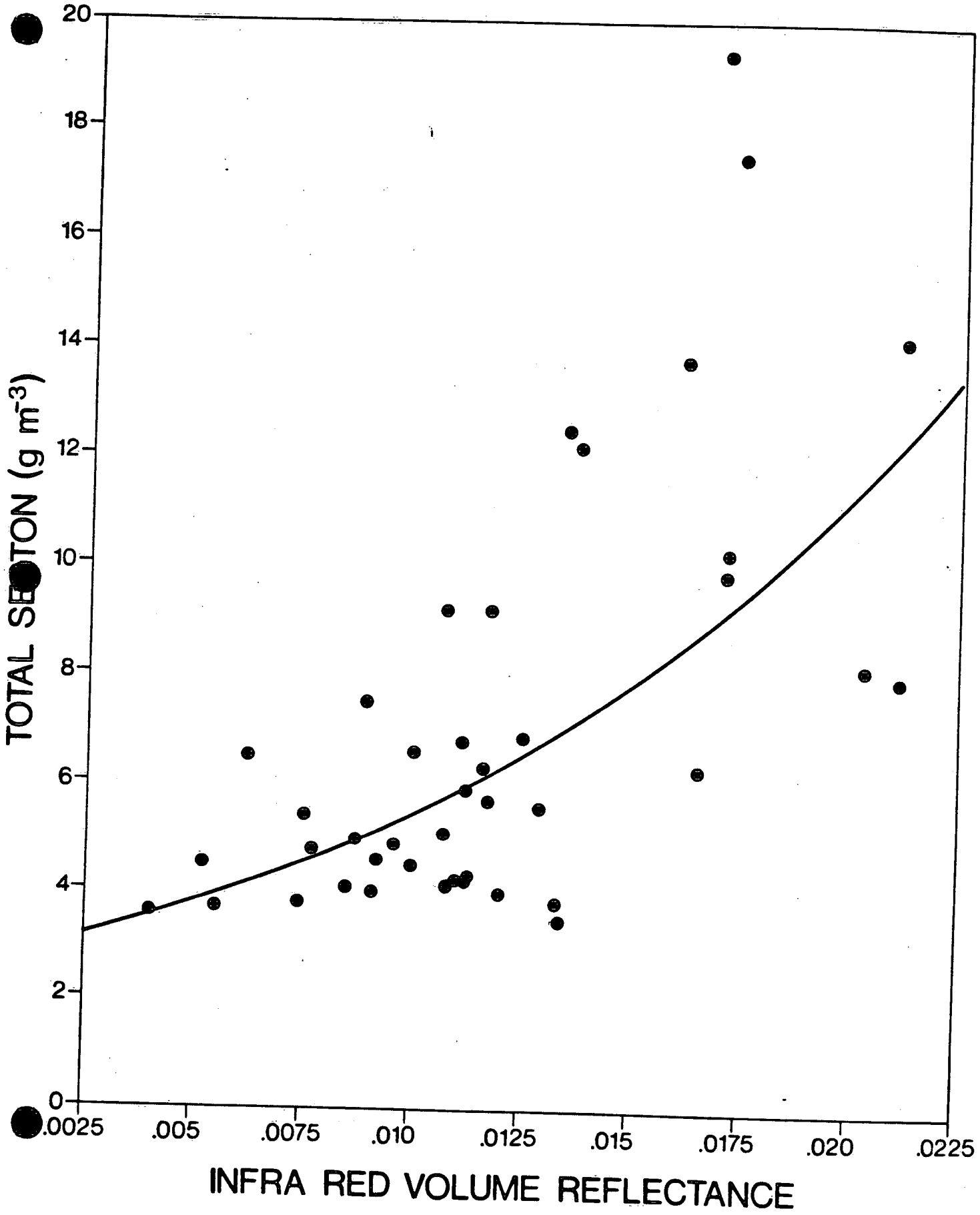
20
18
16
14
12
10
8
6
4
2
0
TOTAL SE TON (g m-3)
.0025
.005
.0075
.010
.0125
.015
.0175
.020
.0225
INFRA RED VOLUME REFLECTANCE

FIG. 20

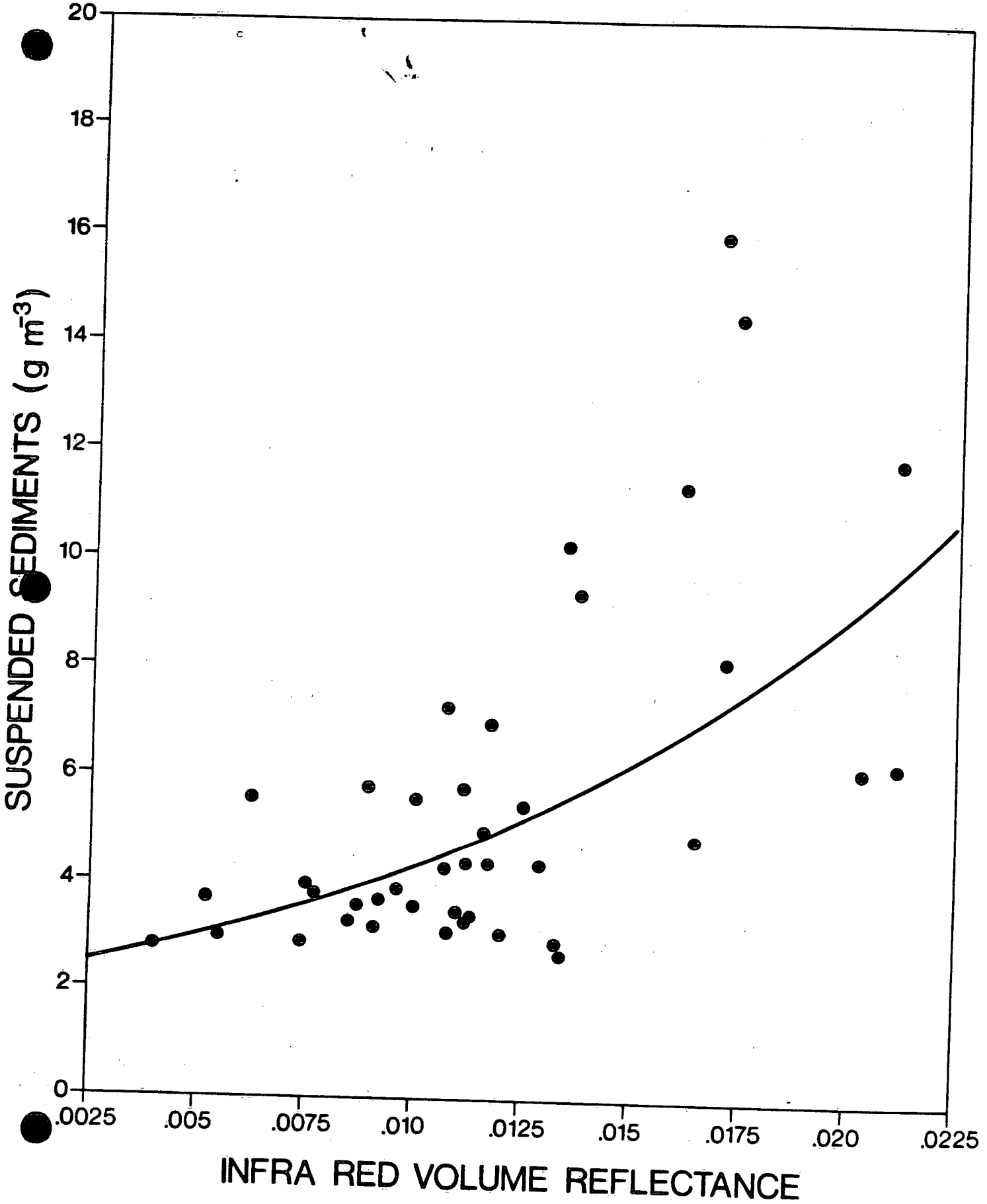
20
18
16
14
12
10
8
6
4
2
0
SUSPENDED SEDIMENTS (g m^{-3})
.0025
.005
.0075
.010
.0125
.015
.0175
.020
.0225
INFRA RED VOLUME REFLECTANCE

FIG. 21

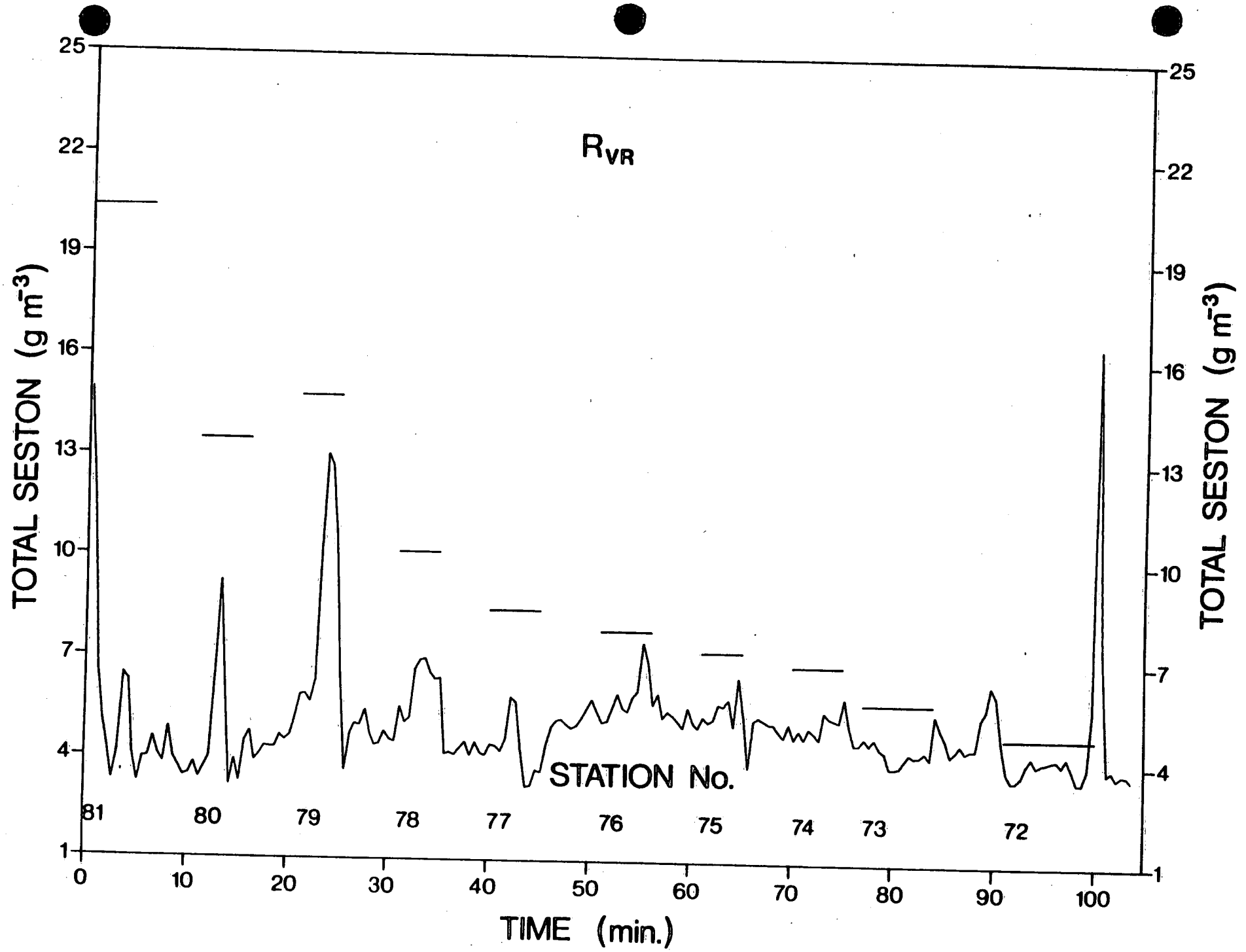
R_{VR}
TOTAL SESTON (g m^{-3})
TOTAL SESTON (g m^{-3})
25
22
19
16
13
10
7
4
1
STATION No.
81
80
79
78
77
76
75
74
73
72
0
10
20
30
40
50
60
70
80
90
100
TIME (min.)

FIG. 22

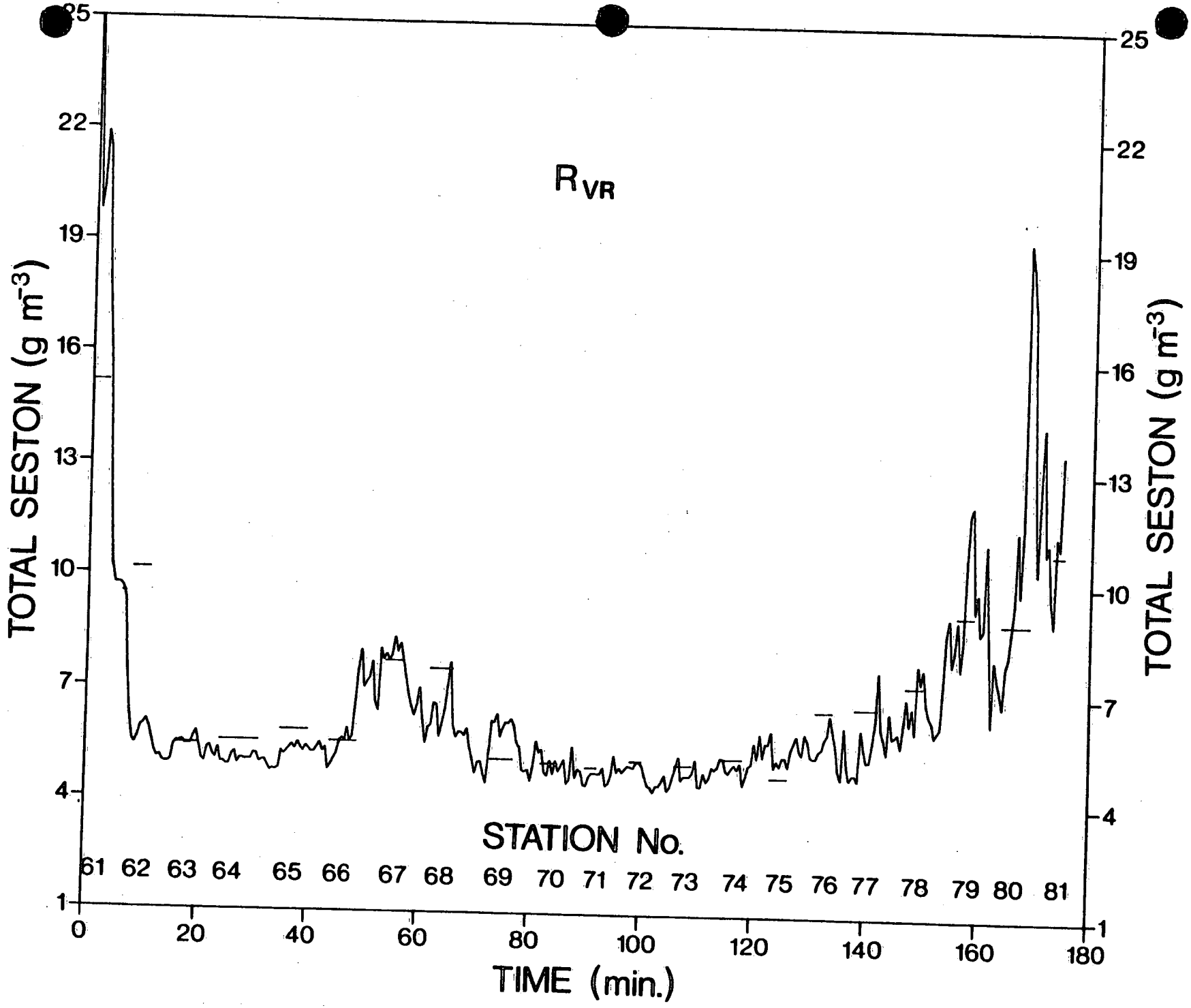
R VR
TOTAL SESTON (g m-3)
TOTAL SESTON (g m-3)
25
22
19
16
13
10
7
4
1
STATION No.
61 62 63 64 65 66 67 68 69 70 71 72 73 74 75 76 77 78 79 80 81
0 20 40 60 80 100 120 140 160 180
TIME (min.)

FIG. 23

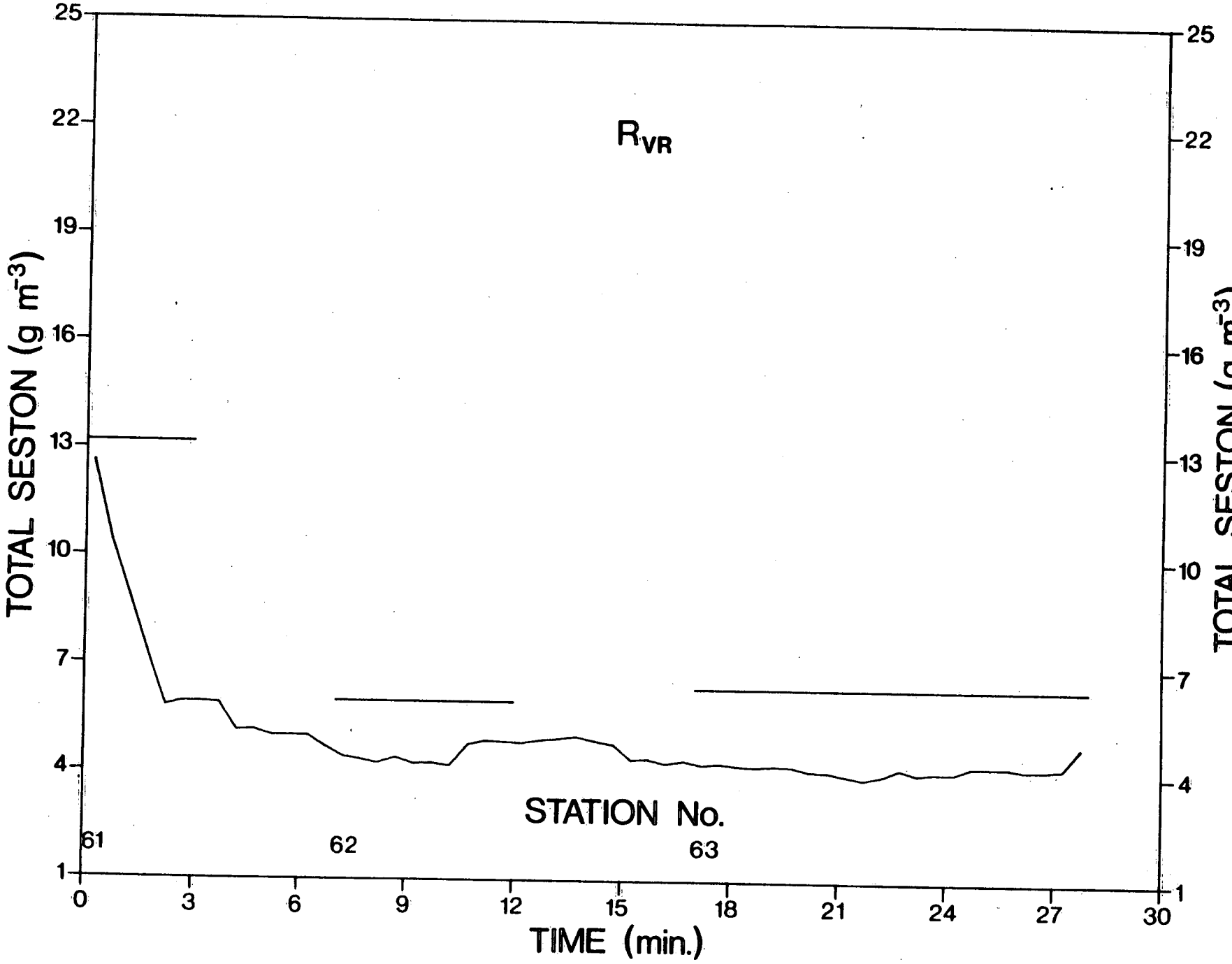
R_{VR}
TOTAL SESTON (g m^{-3})
25
22
19
16
13
10
7
4
1
STATION No.
61
62
63
0
3
6
9
12
15
18
21
24
27
30
TIME (min.)

FIG. 24

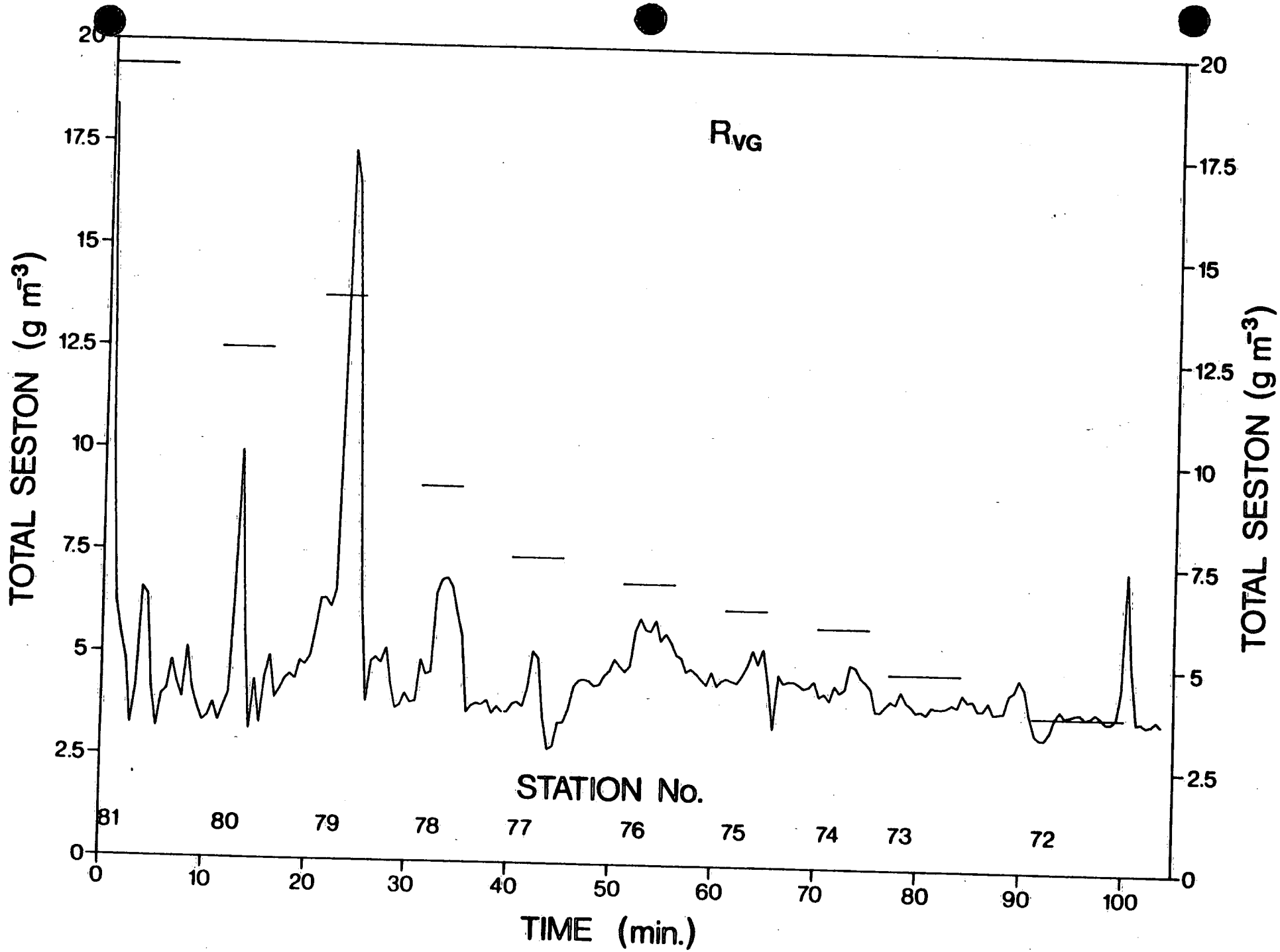
R_{VG}
TOTAL SESTON (g m^{-3})
TOTAL SESTON (g m^{-3})
0
2.5
5
7.5
10
12.5
15
17.5
20
STATION No.
81
80
79
78
77
76
75
74
73
72
0
10
20
30
40
50
60
70
80
90
100
TIME (min.)

FIG. 25

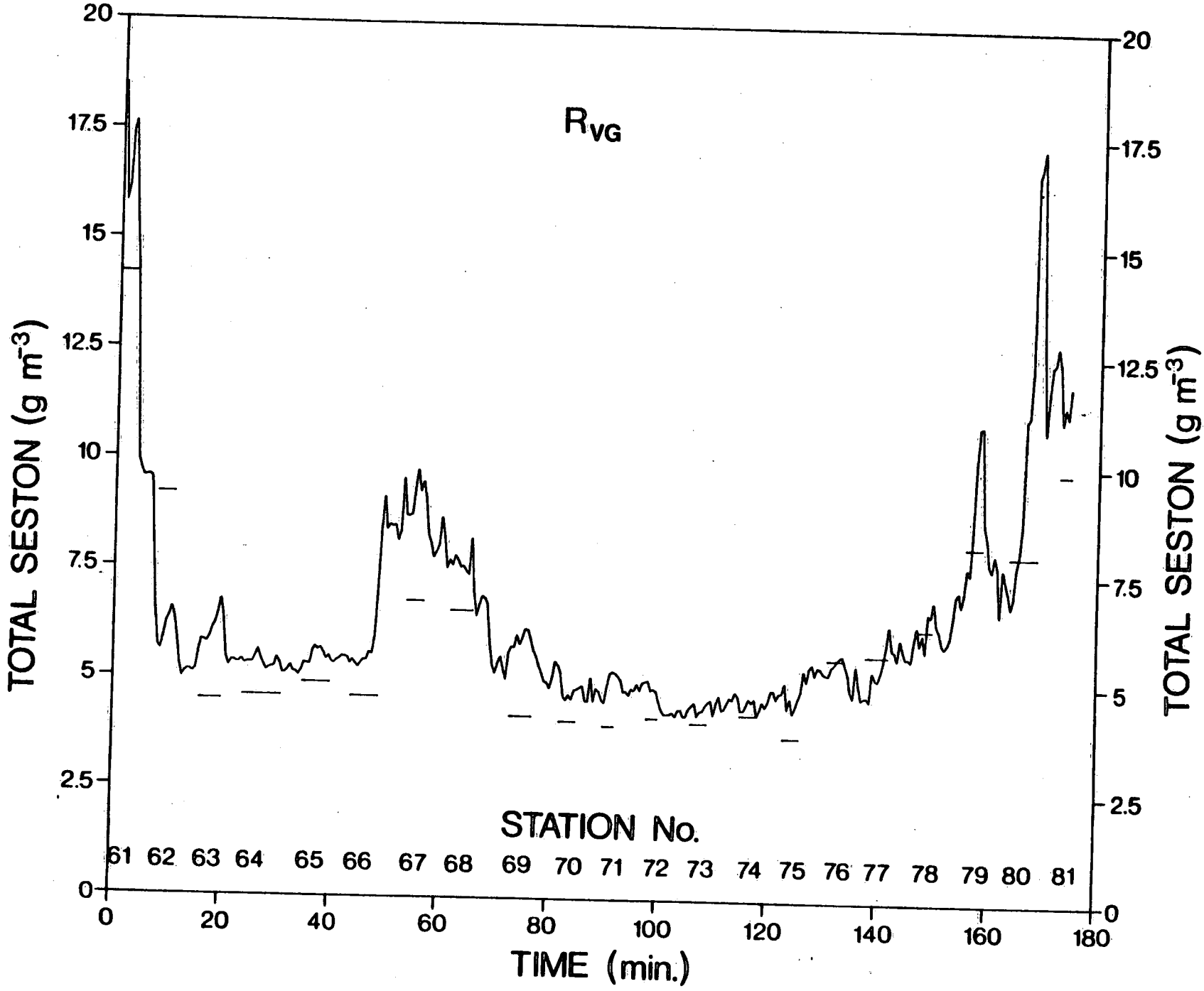
R_{VG}
TOTAL SESTON (g m^{-3})
TOTAL SESTON (g m^{-3})
20
17.5
15
12.5
10
7.5
5
2.5
0
STATION No.
61 62 63 64 65 66 67 68 69 70 71 72 73 74 75 76 77 78 79 80 81
0 20 40 60 80 100 120 140 160 180
TIME (min.)

FIG. 26

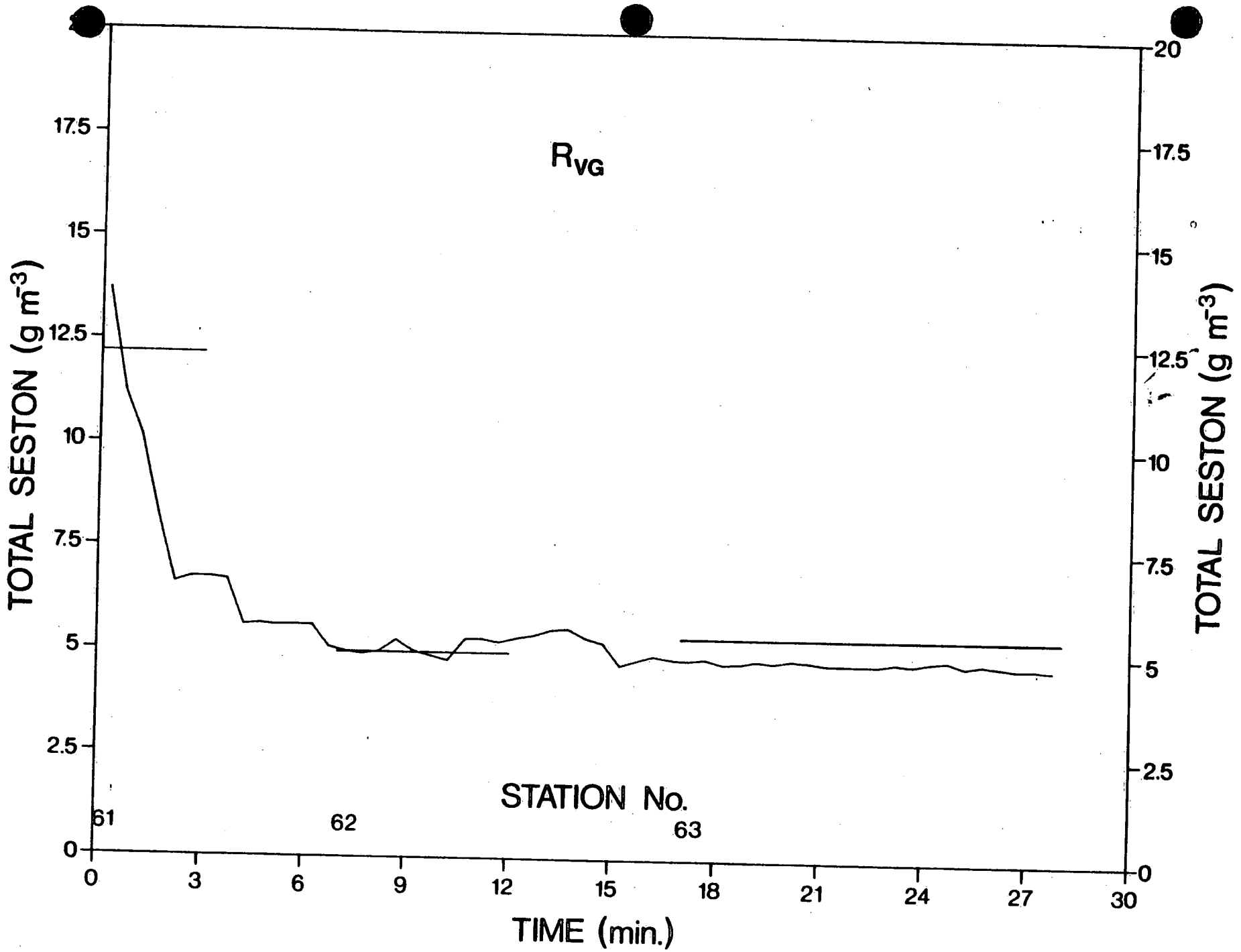
R_{VG}
TOTAL SESTON (g m^{-3})
TOTAL SESTON (g m^{-3})
0
2.5
5
7.5
10
12.5
15
17.5
20
STATION No.
61
62
63
0
3
6
9
12
15
18
21
24
27
30
TIME (min.)

FIG. 27

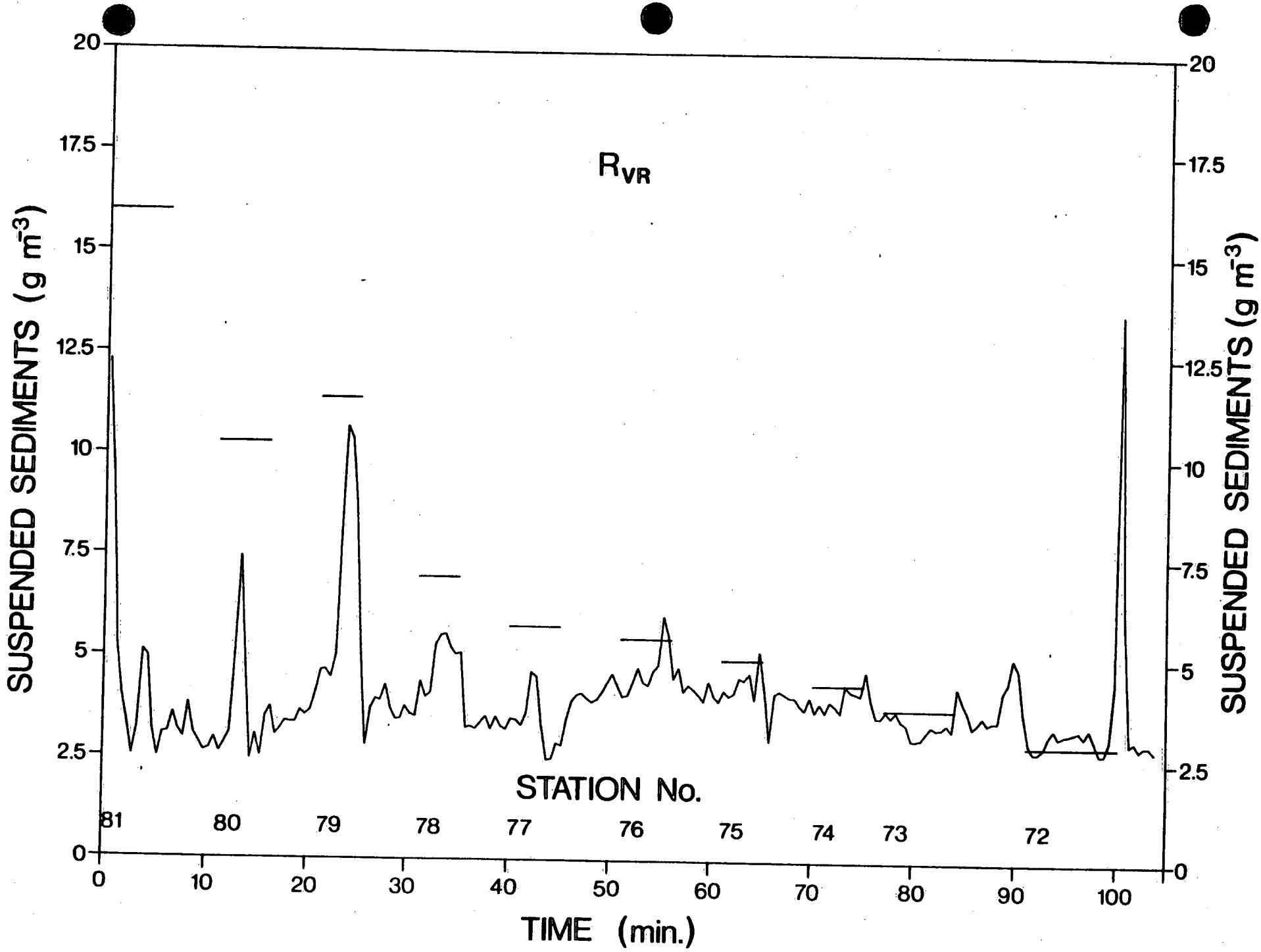
R_{VR}
SUSPENDED SEDIMENTS (g m^{-3})
SUSPENDED SEDIMENTS (g m^{-3})
20
17.5
15
12.5
10
7.5
5
2.5
0
STATION No.
81
80
79
78
77
76
75
74
73
72
0
10
20
30
40
50
60
70
80
90
100
TIME (min.)

FIG. 28

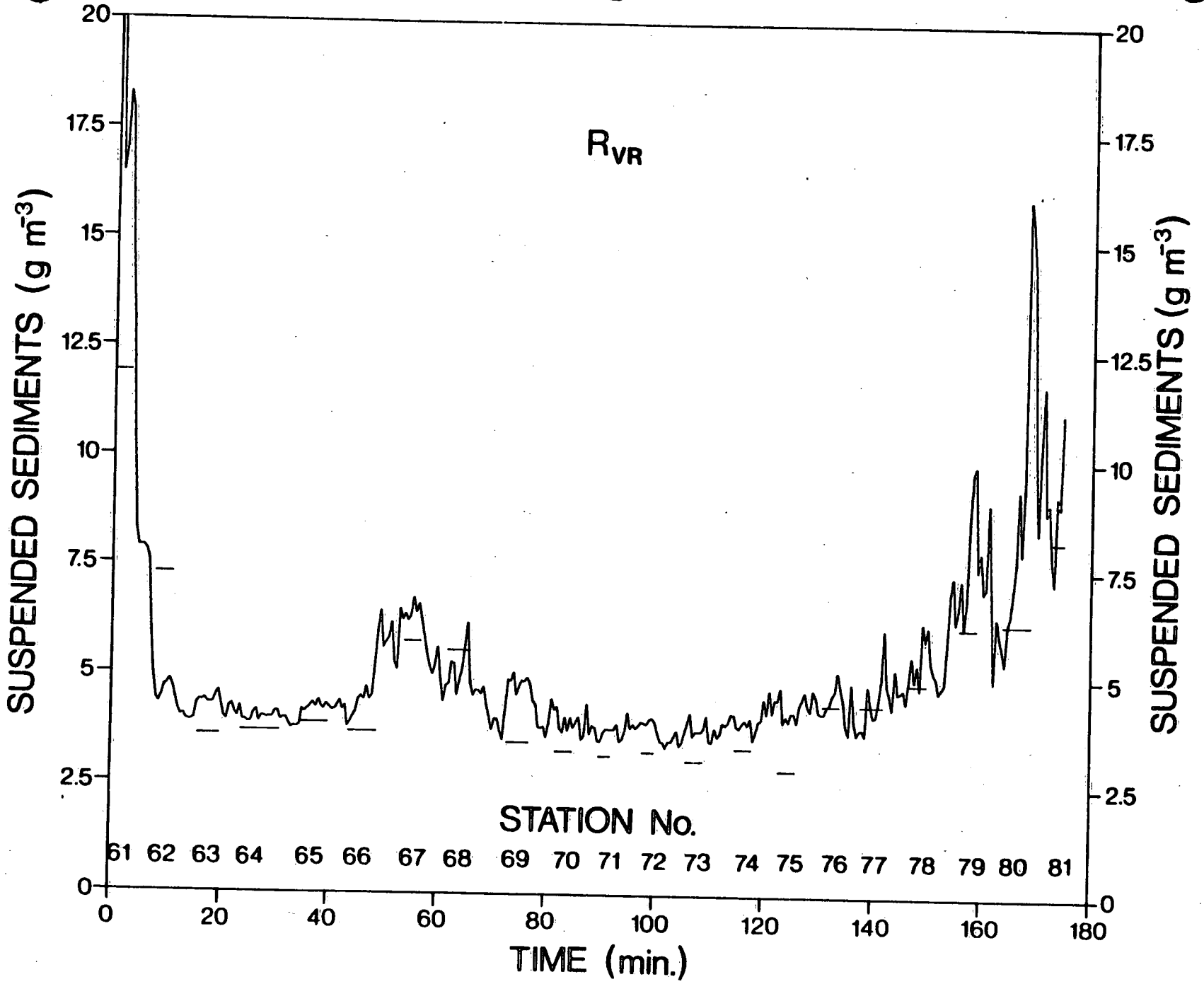
R_{VR}
SUSPENDED SEDIMENTS (g m^{-3})
SUSPENDED SEDIMENTS (g m^{-3})
20
17.5
15
12.5
10
7.5
5
2.5
0
STATION No.
61 62 63 64 65 66 67 68 69 70 71 72 73 74 75 76 77 78 79 80 81
0 20 40 60 80 100 120 140 160 180
TIME (min.)

FIG. 29

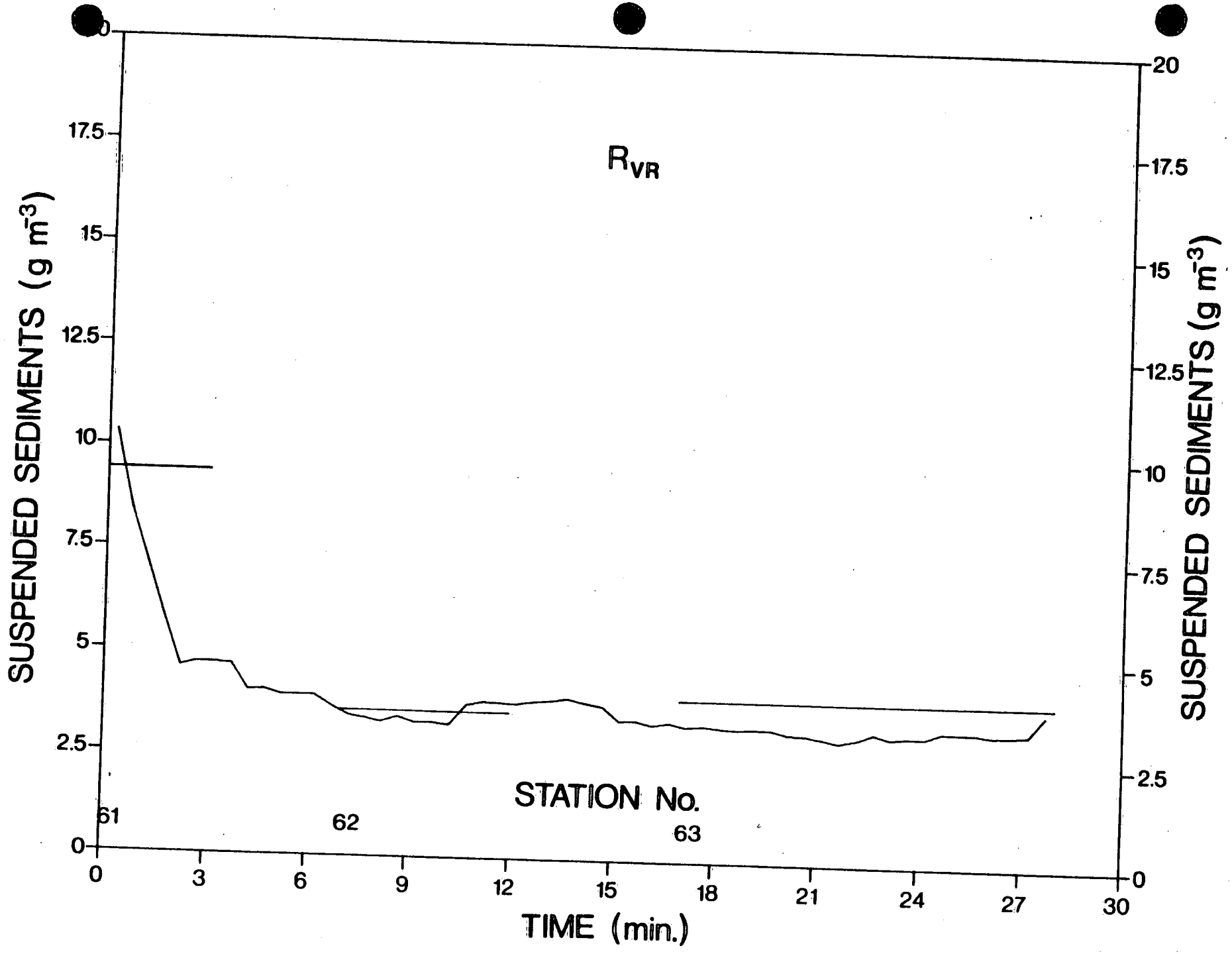
R_{VR}
SUSPENDED SEDIMENTS (g m^{-3})
SUSPENDED SEDIMENTS (g m^{-3})
0
2.5
5
7.5
10
12.5
15
17.5
20
STATION No.
61
62
63
0
3
6
9
12
15
18
21
24
27
30
TIME (min.)

FIG. 30

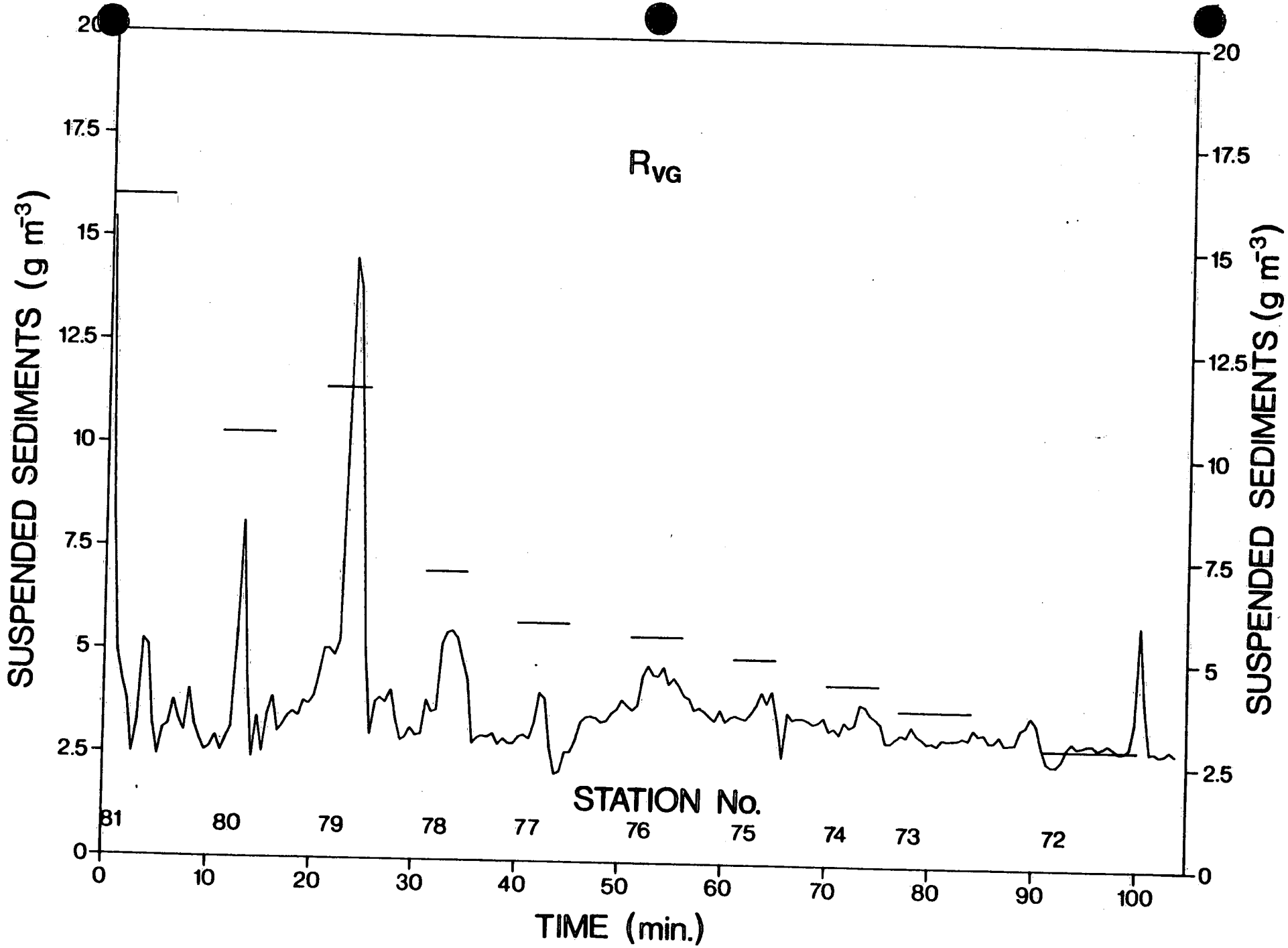
R_VG
SUSPENDED SEDIMENTS (g m⁻³)
SUSPENDED SEDIMENTS (g m⁻³)
0
2.5
5
7.5
10
12.5
15
17.5
20
STATION No.
81
80
79
78
77
76
75
74
73
72
0
10
20
30
40
50
60
70
80
90
100
TIME (min.)

FIG. 31

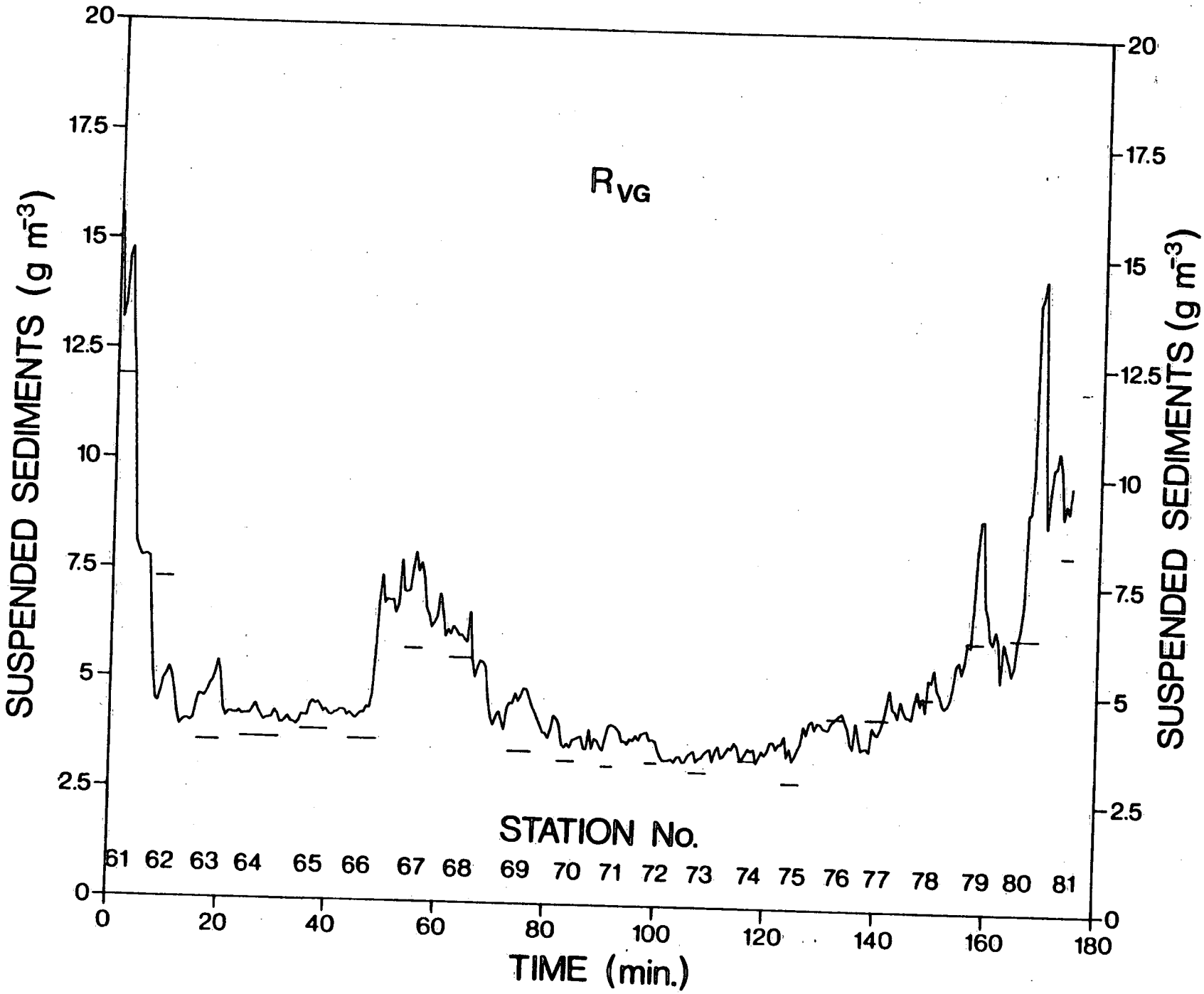
R VG
SUSPENDED SEDIMENTS (g m-3)
SUSPENDED SEDIMENTS (g m-3)
20
17.5
15
12.5
10
7.5
5
2.5
0
STATION No.
61 62 63 64 65 66 67 68 69 70 71 72 73 74 75 76 77 78 79 80 81
0 20 40 60 80 100 120 140 160 180
TIME (min.)

FIG. 32

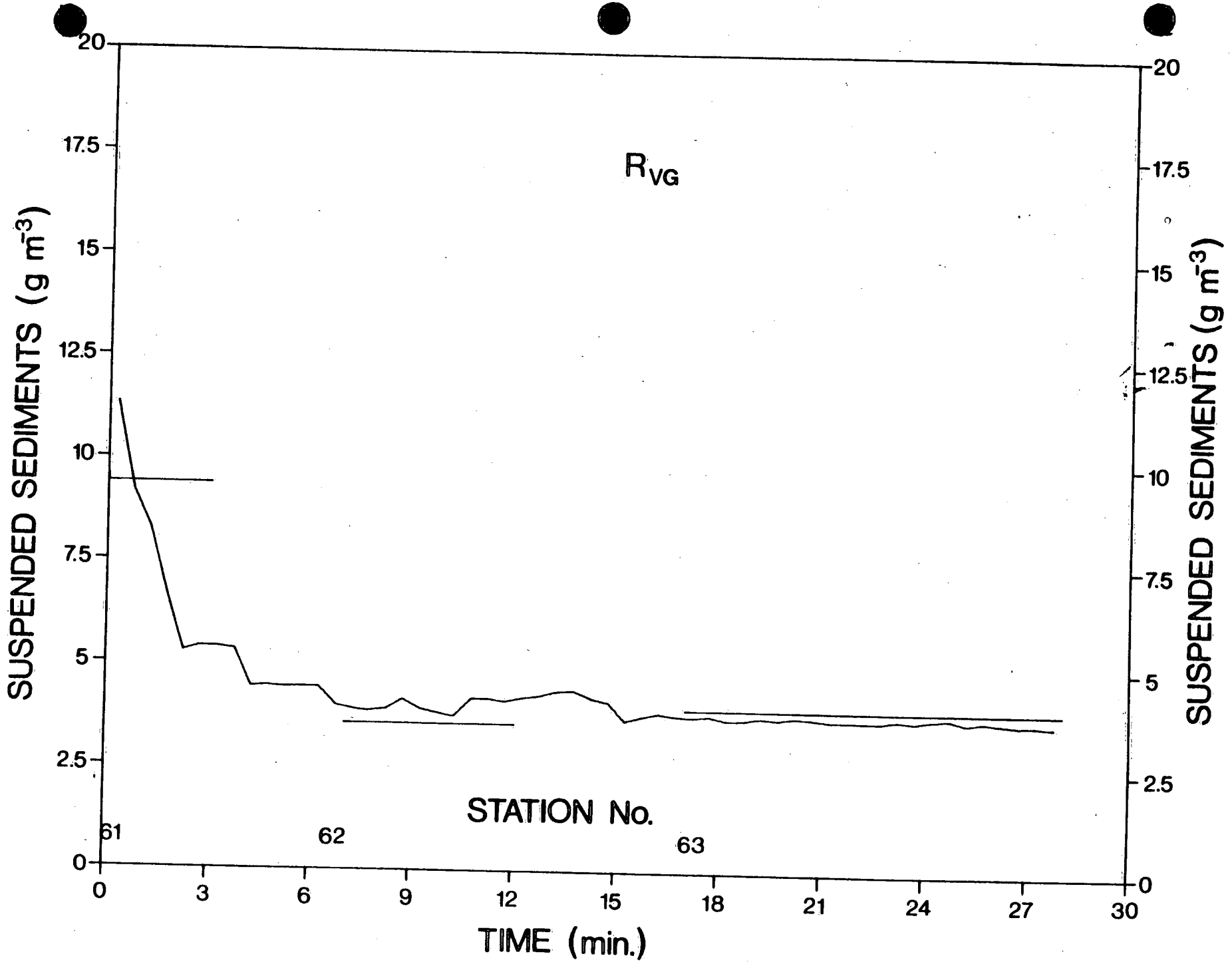
R_{VG}
SUSPENDED SEDIMENTS (g m^{-3})
SUSPENDED SEDIMENTS (g m^{-3})
20
17.5
15
12.5
10
7.5
5
2.5
0
STATION No.
61
62
63
0
3
6
9
12
15
18
21
24
27
30
TIME (min.)

FIG. 33

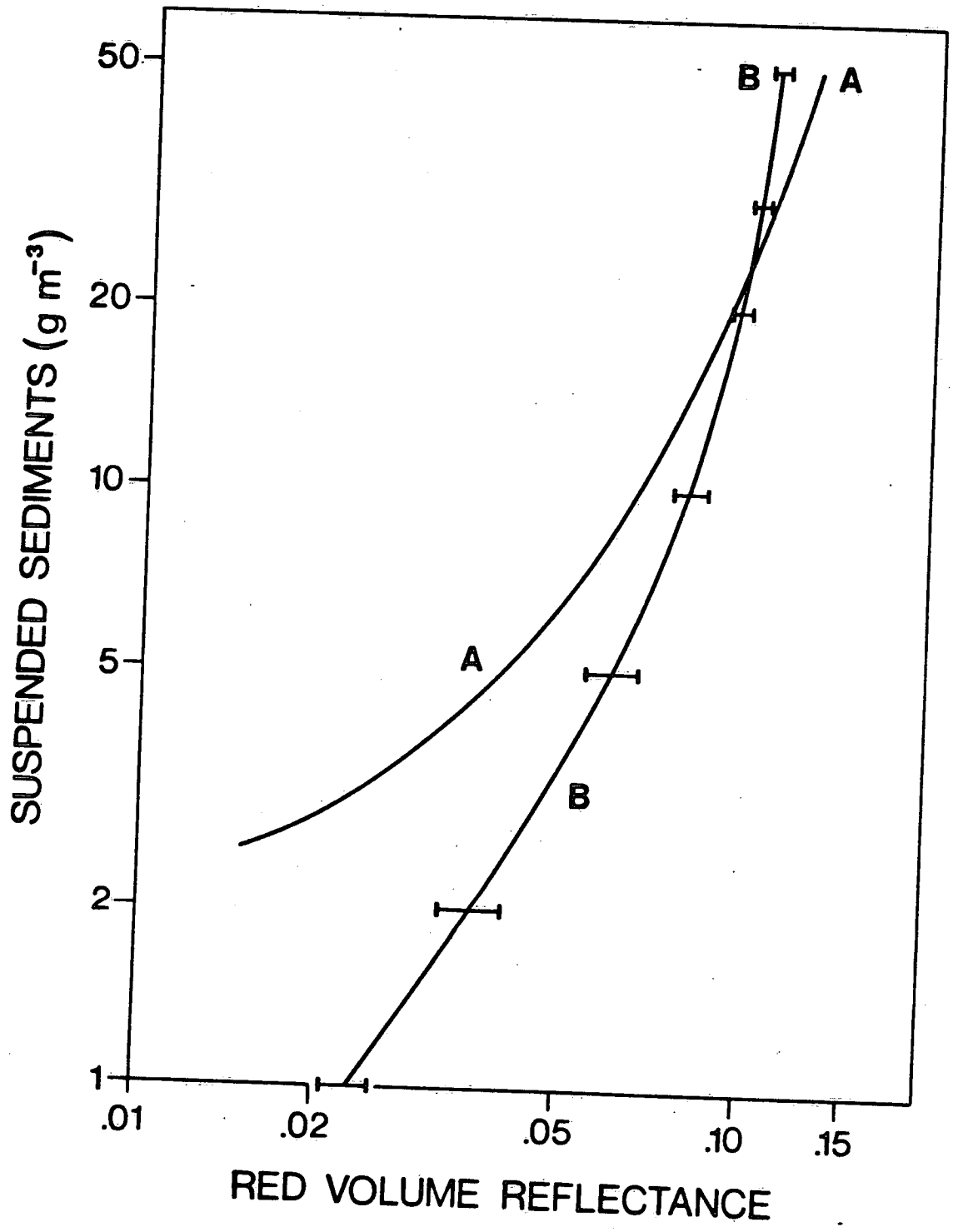
50
20
10
5
2
1
SUSPENDED SEDIMENTS (g m⁻³)
B
A
A
B
.01
.02
.05
.10
.15
RED VOLUME REFLECTANCE

FIG. 34